INTERNATIONAL JOURNAL FOR NUMERICAL METHODS IN ENGINEERING
Int. J. Numer. Meth. Engng 2011; **87**:232–261
Published online 28 October 2010 in Wiley Online Library (wileyonlinelibrary.com). DOI: 10.1002/nme.3036

Implicit Large Eddy Simulation of transition to turbulence at low Reynolds numbers using a Discontinuous Galerkin method

A. Uranga[1], P.-O. Persson[2], M. Drela[1] and J. Peraire[1,*,†]

[1]*Department of Aeronautics and Astronautics, Massachusetts Institute of Technology, Cambridge, MA, U.S.A.*
[2]*Department of Mathematics, University of California Berkeley, Berkeley, CA, U.S.A.*

SUMMARY

The present work predicts the formation of laminar separation bubbles at low Reynolds numbers and the related transition to turbulence by means of Implicit Large Eddy Simulations with a high-order Discontinuous Galerkin method. The flow around an SD7003 infinite wing at an angle of attack of 4° is considered at Reynolds numbers of 10 000, 22 000, and 60 000 in order to gain insight into the characteristics of the laminar and turbulent regimes. At the lowest Reynolds number studied, the flow remains laminar and two dimensional over the wing surface, with a periodic vortex shedding. For higher Reynolds numbers, the flow is unsteady over the upper wing surface and exhibits a separation bubble along which the flow transitions to turbulence. Tollmien–Schlichting (TS) waves are observed in the boundary layer, and transition is found to be caused by unstable TS modes as revealed by the growth of the stream-wise amplification factor. Copyright © 2010 John Wiley & Sons, Ltd.

Received 16 March 2010; Revised 29 June 2010; Accepted 1 July 2010

KEY WORDS: Discontinuous Galerkin method; Implicit Large Eddy Simulation; transition to turbulence; laminar separation bubble; low Reynolds number

Dedicated to the memory of O. C. Zienkiewicz

1. INTRODUCTION

Interest in micro-air vehicles (MAVs) has grown considerably in the last decades stimulated by the miniaturization of technology and the advancements in micro systems. The recent years have also seen an increasing interest in animal locomotion: fish swimming, bird flying, and insect flapping have been studied both by engineers and biologists. Animal locomotion is interesting from the point of view of design of small flying vehicles, and also from a fundamental physics and engineering perspective. As for MAVs, the flows encountered are in the so-called low Reynolds number regime, with Reynolds numbers between 10^3 and 10^5.

In this regime, the location of transition to turbulence has a significant impact on aerodynamic performance. Laminar flows have a much greater tendency to undergo detrimental separation than the essentially turbulent flows encountered at high Reynolds numbers. Furthermore, if the flow separates, the transition location determines whether the flow reattaches or not, and the impact of separation on lift and drag. Hence, accurately predicting transition is of crucial importance in the simulation of low Reynolds number flows.

*Correspondence to: J. Peraire, Department of Aeronautics and Astronautics, Massachusetts Institute of Technology, 77 Massachusetts Ave, Room 37-451, Cambridge, MA 02139, U.S.A.
†E-mail: peraire@mit.edu

In addition, simulating the flows encountered in MAVs and those related to the swimming of fish or the flapping of bats represents a significant challenge for fluid flow computations. The flows are highly unstable, with laminar, transitional, and turbulent regions. In the presence of an adverse pressure gradient, a laminar boundary layer can separate and subsequently reattach, thus forming a laminar separation bubble (LSB). Separation, transition, and reattachment can take place over a significantly short distance, and the bubble can fluctuate in size and position.

The present work thus focuses on two important aspects related to the simulation of low Reynolds number flows, which require further understanding, namely the transition mechanism and related problem of transition prediction, and the feasibility of numerical simulations to predict the flows involved. The problem considered here is that of predicting the formation of an LSB and the transition to turbulence in the three-dimensional flow around an SD7003 infinite wing section at an angle of attack of 4° and Reynolds numbers of 10 000, 22 000, and 60 000. We expand our preliminary results [1] by considering a more comprehensive set of cases and employing finer meshes.

Several studies have shown that transition to turbulence can be predicted by means of Large Eddy Simulations (LES) [2–4]. Furthermore, the accurate simulation of transition requires low numerical dispersion and dissipation. Thus, we have chosen to use a high-order Discontinuous Galerkin (DG) finite-element method as it combines high accuracy with the geometric flexibility required for practical applications.

The DG method has only been used for LES by few research groups, mostly for two-dimensional or periodic simulations: fully developed channel flow [5, 6], two-dimensional channel flow [7], two-dimensional mixing layer and a back-facing step [8]. To the authors knowledge, the preliminary results we presented previously [1] together with the present investigation constitute the first attempt at using a DG method for fully three-dimensional implicit LES.

The DG method provides many of the advantages of finite-element methods while retaining the main strengths of finite-volume methods for conservation laws. In particular, it relies upon a strong mathematical foundation and allows for high-order implementations, while being able to handle complex geometries and grid adaptation with unstructured grids. In addition, it provides local conservation and a stable discretization of the convective operator.

On the other hand, the DG approach requires significantly more operations per computational cell than finite differences and finite volumes. This is only partly offset by the use of high-order representations of the solution—typically third- to fifth-order polynomial representations being used in practice. There is clearly some work to be done to make DG methods more computationally efficient, but the advantages of DG and the potential for overcoming some of the limitations of other methods seem to justify the effort.

2. BACKGROUND

Studies of the transition to turbulence in conjunction with an LSB provide the following scenario: in the attached flow, the magnitude of Tollmien–Schlichting (TS) waves is amplified, as in the classical cases of natural transition; in the separated shear layer, Kelvin–Helmholtz (KH) instabilities are rapidly amplified, leading to the development of three-dimensional vortices and eventually to the breakdown to turbulence; the now turbulent flow reattaches to the wall, thus closing the separation bubble [9–11].

Thus, the transition location along a separation bubble determines the bubble's size: rapid transition induces rapid reattachment, whereas delayed transition results in a longer separation bubble. In turn, an airfoil's aerodynamic characteristics, such as drag, are very sensitive to the bubble length [12] and hence to the transition location. An LSB can form on the suction side of airfoils at low Reynolds numbers and large angles of attack, when the stable vortex street observed at somewhat lower angles or lower Reynolds numbers becomes unstable and causes the separated boundary layer to reattach.

Low Reynolds number studies of separation bubbles on airfoils and wings often make use of the SD7003 profile [13, 14] shown in Figure 1, since it exhibits an LSB on the upper surface that

DOI: 10.1002/nme

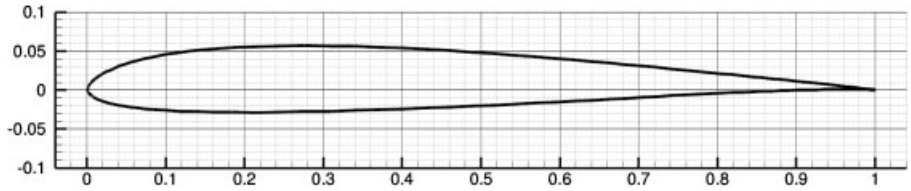

Figure 1. SD7003 airfoil: 8.51% maximum thickness, 1.46% camber.

is present over a range of Reynolds numbers and angles of attack. The flow around a rectangular SD7003 wing at Reynolds number 60 000 and 4° angle of attack has been studied experimentally using particle-image velocimetry (PIV) in several facilities, thus providing a good database for validation. The comparison by Ol *et al.* [15] focuses on contours of mean velocity and Reynolds stresses, as well as on separation, transition, and reattachment locations. This same flow was also studied computationally by several groups. Tang [16] employs several models for RANS simulations, whereas Lian and Shyy [17] make use of the standard $k-\omega$ RANS model in conjunction with an e^N transition module.

Three-dimensional Implicit Large Eddy Simulations (ILES) were carried out by Visbal and collaborators using a sixth-order accurate compact difference code [3, 4]. They studied the flow at different angles of attack ranging between 2 and 14° and for Reynolds numbers between 10 000 and 90 000. They observed that the LSB decreases in size and moves closer to the leading-edge with either increasing angle of attack or increasing Reynolds number. No transition was observed for Reynolds numbers of and below 40 000, while the size of the turbulent flow structures was verified to decrease with increasing Reynolds number. In another paper [18], a linear stability study for the $Re=60000$ case at 4° angle of attack is presented using as base flow the time-averaged flow of unsteady ILES. The unstable disturbances are found to be confined to the LSB with maximum magnitude and maximum gradient at the center of the bubble, which is consistent with the Reynolds stress contours previously presented.

Hain *et al.* focused on the transition mechanism in an experimental investigation of the 66 000 Reynolds number flow around an SD7003 rectangular wing using time-resolved PIV [11]. They show that transition is dominated by KH instabilities in the separated shear layer, which, in some cases, have almost the same unstable frequency than the TS instabilities developing before separation. They thus conclude that the TS waves trigger the amplification of the KH waves, which explains why the size of the separation bubble is affected by the magnitude of the TS waves at separation.

3. COMPUTATIONAL METHODOLOGY

3.1. Governing equations

The motion of a compressible Newtonian fluid is governed by the Navier–Stokes equations, which express the conservation of mass, momentum, and energy as

$$\frac{\partial \rho}{\partial t}+\frac{\partial}{\partial x_i}(\rho u_i)=0, \tag{1}$$

$$\frac{\partial}{\partial t}(\rho u_i)+\frac{\partial}{\partial x_j}(\rho u_i u_j)=-\frac{\partial p}{\partial x_i}+\frac{\partial \tau_{ij}}{\partial x_j} \quad \text{for } i\in\{1,2,3\}, \tag{2}$$

$$\frac{\partial}{\partial t}(\rho E)+\frac{\partial}{\partial x_j}[u_j(\rho E+p)]=-\frac{\partial q_j}{\partial x_j}+\frac{\partial}{\partial x_j}(u_i\tau_{ij}), \tag{3}$$

DOI: 10.1002/nme

where the viscous stress tensor, τ_{ij}, and the heat flux, q_i, are given by, respectively,

$$\tau_{ij} \equiv \mu \left[\left(\frac{\partial u_i}{\partial x_j} + \frac{\partial u_j}{\partial x_i} \right) - \frac{2}{3} \frac{\partial u_k}{\partial x_k} \delta_{ij} \right], \tag{4}$$

$$q_j \equiv - \frac{\mu}{Pr} \frac{\partial}{\partial x_j} \left(E + \frac{p}{\rho} - \frac{1}{2} u_k u_k \right). \tag{5}$$

In the above equations, ρ denotes the fluid density, u_i the velocity component in the direction x_i, p the static pressure, E the total energy per unit mass, μ the dynamic viscosity coefficient, and Pr the flow Prandtl number assumed to be constant. The system is closed with the ideal gas equation of state written in the form

$$p = (\gamma - 1) \rho \left(E - \tfrac{1}{2} u_k u_k \right). \tag{6}$$

For all the flows considered in the present work, the specific heat ratio is set to $\gamma = 1.4$ and the Prandtl number to $Pr = 0.72$. Moreover, the kinematic viscosity, $\nu = \mu / \rho$, is assumed to be constant since only low Mach number flows are considered.

3.2. Turbulence modeling

In the present work, the ILES approach is followed and the unresolved small eddies are accounted for by means of numerical dissipation. Thus, no subgrid-scale (SGS) model is employed and the full (unfiltered) compressible Navier–Stokes equations are solved. This approach has been successfully used by Visbal and collaborators using a compact difference method to simulate the flow around an SD7003 airfoil [3, 4].

In an LES, the large-scale motions are resolved whereas the small scales are modeled. The principle behind LES is justified by the fact that the larger scales, because of their size and strength, carry most of the flow energy while being responsible for most of the transport, and therefore should be simulated precisely (i.e. resolved). On the other hand, the small scales have relatively little influence on the mean flow and thus can be approximated (i.e. modeled). Furthermore, they tend to be more homogeneous and isotropic and hence are easier to model than the large scales.

Owing to the non-linear nature of the Navier–Stokes equations, all turbulent scales are dynamically coupled. Hence, for the resolved scales to be dynamically accurate, the effect of the SGSs needs to be taken into account, either with an SGS model in the standard (explicit) LES approach, or via numerical dissipation in ILES. Much effort was put for a number of years on deriving better SGS models in particular in the 1990s [19, 20], but eventually Spalart's conclusion that 'there is little to gain by refining the SGS models' [21] became shared by more and more authors, e.g. [22].

An alternative is to use the numerical dissipation of the solution scheme to account for the dissipation that would take place in the unresolved scales. The first ILES approach was thus introduced in 1990 by Boris and his collaborators at the Naval Research Laboratory [23]. The truncation errors that stem from the numerical procedure amount to an implicit SGS model; this can be shown through qualitative, physical considerations, or by making use of modified equation analysis to quantify the errors of the numerical algorithm. It is possible to show that a numerical method solves a certain differential equation more accurately than the original equation, and that for certain methods 'leading-order truncation error terms introduced provide implicit SGS models similar in form to those of the conventional mixed SGS models' [24] (see also [25–29]).

The ILES development and success has emphasized the importance of choosing numerical methods that are built upon the physics of the flow rather than simply considering them as approximations [30]. The absence of an explicit SGS model equation also makes this approach easy to implement and decreases the computational cost. Since an LES shows more structures and provides a more accurate answer as the grid is refined, one seems to be better off paying a computational cost to increase the resolution than to solve an extra equation [23].

DOI: 10.1002/nme

3.3. Discontinuous Galerkin method

The modeling Equations (1)–(6) are solved using a high-order DG finite-element method implemented in the computational code *3DG*. This framework solves time-dependent systems of conservation laws of the form

$$\begin{aligned} &\frac{\partial \mathbf{u}}{\partial t} + \nabla \cdot \mathbf{F}_i(\mathbf{u}) - \nabla \cdot \mathbf{F}_v(\mathbf{u}, \mathbf{q}) = \mathbf{S}(\mathbf{u}, \mathbf{q}), \\ &\mathbf{q} - \nabla \mathbf{u} = 0, \end{aligned} \tag{7}$$

in a domain Ω, with conserved state variables $\mathbf{u}$, inviscid flux function $\mathbf{F}_i$, viscous flux function $\mathbf{F}_v$, and source term $\mathbf{S}$.

We consider a triangulation $\mathscr{T}_h$ of the spatial domain Ω and introduce the spaces

$$V_h = \{\mathbf{v} \in [L^2(\Omega)]^m | \mathbf{v}|_K \in [\mathscr{P}_p(K)]^m, \ \forall K \in \mathscr{T}_h\},$$

$$\Sigma_h = \{\mathbf{r} \in [L^2(\Omega)]^{dm} | \mathbf{r}|_K \in [\mathscr{P}_p(K)]^{dm}, \ \forall K \in \mathscr{T}_h\},$$

where $\mathscr{P}_p(K)$ is the space of polynomial functions of degree at most $p \geqslant 0$ on element K, m is the dimension of $\mathbf{u}$ (i.e. number of independent flow variables or states), and d is the spatial dimension. The DG formulation is then: find $\mathbf{u}_h \in V_h$ and $\mathbf{q}_h \in \Sigma_h$ such that for all $K \in \mathscr{T}_h$,

$$\int_K \mathbf{q}_h \cdot \mathbf{r} \, \mathrm{d}x = -\int_K \mathbf{u}_h \nabla \cdot \mathbf{r} \, \mathrm{d}x + \int_{\partial K} \hat{\mathbf{u}} \mathbf{r} \cdot \mathbf{n} \, \mathrm{d}s \quad \forall \mathbf{r} \in [\mathscr{P}_p(K)]^{dm},$$

$$\begin{aligned} &\int_K \frac{\partial \mathbf{u}_h}{\partial t} \mathbf{v} \, \mathrm{d}x - \int_K [\mathbf{F}_i(\mathbf{u}_h) - \mathbf{F}_v(\mathbf{u}_h, \mathbf{q}_h)] \cdot \nabla \mathbf{v} \, \mathrm{d}x \\ &\quad = \int_K \mathbf{S}(\mathbf{u}_h, \mathbf{q}_h) \mathbf{v} \, dx - \int_{\partial K} [\hat{\mathbf{F}}_i - \hat{\mathbf{F}}_v] \cdot \mathbf{n} \mathbf{v} \, \mathrm{d}s \quad \forall \mathbf{v} \in [\mathscr{P}_p(K)]^m. \end{aligned}$$

Here, the numerical fluxes $\hat{\mathbf{F}}_i$, $\hat{\mathbf{F}}_v$, and $\hat{\mathbf{u}}$ are approximations to $\mathbf{F}_i$, $\mathbf{F}_v$, and $\mathbf{u}$, respectively, on the boundary ∂K of element K. The DG formulation is complete once these numerical fluxes are specified in terms of $\mathbf{q}_h$ and $\mathbf{u}_h$, and the boundary conditions are enforced.

The inviscid flux $\hat{\mathbf{F}}_i$ is determined with Roe's scheme [31] and provides the numerical dissipation needed for ILES. The viscous flux $\hat{\mathbf{F}}_i$ is calculated using the Compact Discontinuous Galerkin (CDG) method introduced by Peraire and Persson [32]: by choosing the numerical flux $\hat{\mathbf{u}}$ to be a function of $\mathbf{u}_h$ and not $\mathbf{q}_h$, the degrees of freedom associated with $\mathbf{q}_h$ can be eliminated after discretization at the element level, which results in a system involving only the degrees of freedom corresponding to the conserved variables $\mathbf{u}_h$. The final result is a system of coupled ordinary differential equations of the form

$$\boldsymbol{M}\dot{\boldsymbol{u}} = \boldsymbol{R}(\boldsymbol{u}), \tag{8}$$

where $\boldsymbol{u}$ is a vector containing the degrees of freedom associated with $\mathbf{u}_h$, and $\dot{\boldsymbol{u}}$ denotes its time derivative. Here, $\boldsymbol{M}$ is the mass matrix and $\boldsymbol{R}$ is the residual vector which is a non-linear function of $\boldsymbol{u}$. Nodal basis expansions are used to represent $\mathbf{u}_h$ inside each element.

The non-linear system of equations is linearized using Newton's method, and the resulting linear system solved with Conjugate Gradient Squared (CGS) preconditioned with incomplete factorizations (ILU) following the work by Persson and Peraire [33]. The code is parallelized using a domain decomposition approach with partition-wise ILU factorizations, the details of which can be found in the paper by Persson [34].

3.4. Time stepping scheme and averaging procedure

Time stepping is performed with a two stage, A-stable, third-order accurate diagonal implicit Runge–Kutta (DIRK) method [35]. This allows to take large time steps, and hence the time step

DOI: 10.1002/nme

is chosen only based on physical time resolution considerations and not on numerical stability. Unless otherwise specified, the simulations are performed with a non-dimensional times step of $dt^* = dt \times U_\infty / c = 0.01$, and the solution is saved every five steps for computing statistics and other post-processing ($\Delta t^* = 0.05$).

For all the cases considered, the initial transient is over by $t^* = 15$ as estimated from the forces on the wing. Hence, unless otherwise specified, the average fields, turbulence correlations, and statistics are computed by averaging the solution over a non-dimensional time interval of 10 (that is over 200 solutions for $t^* = [15, 25]$) and then performing a spatial average over 20 span-wise planes.

3.5. Computational domain and grids

The flow around a rectangular wing with an SD7003 airfoil profile at an angle of attack of 4° and free-stream Mach number of 0.2 is considered. Unless otherwise specified, the wing span-to-chord ratio is set to 0.2 following the findings of Galbraith and Visbal [3]. The axes are set up with x being the chord-wise direction and z the span-wise direction, such that the leading-edge is located along the line $x = 0$, $y = 0$.

From the wing's leading-edge line, the domain extends 4.3 chord lengths upstream, 7.4 chord lengths downstream, 5.9 chord lengths above, and 6.0 chord lengths below. Thus, if we denote by c the chord length, the domain has the range $[-4.3c, 7.4c] \times [-6.0c, 5.9c] \times [0, 0.2c]$ along the chord-wise, vertical, and span-wise directions, respectively.

The computational domain has periodic boundary conditions along the span-wise direction in order to simulate an infinite wing. The wing's surface is represented by a non-slip, adiabatic, boundary condition, while a free-stream-type boundary condition employing Roe's approximate Riemann solver is imposed at the outer edges (far-field) of the computational domain.

The grids are constructed by extruding a two-dimensional structured C-mesh around the profile that is generated from a rectangular grid by conformal transformations. To obtain curved elements that are aligned with the geometry boundaries and do not intersect, a fine structured grid is generated and the high-order nodes of the computational mesh are placed at the mesh points of this fine grid. Note that this fine grid is such that the number of subdivisions in each direction is compatible with the number of high-order nodes required for a given polynomial order. The tetrahedral connectivities of the computational mesh are then obtained directly from the cartesian topology of the fine structured grid. The boundaries are thus represented accurately and a high-order mesh appropriate for DG computations is obtained.

We use the term *high-order nodes* to refer to all the nodes used in the numerical procedure at which the variable states are computed, so as to differentiate them from the nodes at the corners of each tetrahedral element.

In order to investigate how much spatial resolution is needed to capture the transition to turbulence that occurs in the separation bubble, three computational grids are considered: a coarse grid (hereafter referred to as grid 1) with 21 504 tetrahedral elements, a medium grid (grid 2) with 52 800 elements, and a fine grid (grid 3) with 85 500 elements. Figures 2 and 3 show the computational grids 1 and 2 on a planar cut along the span-wise direction.

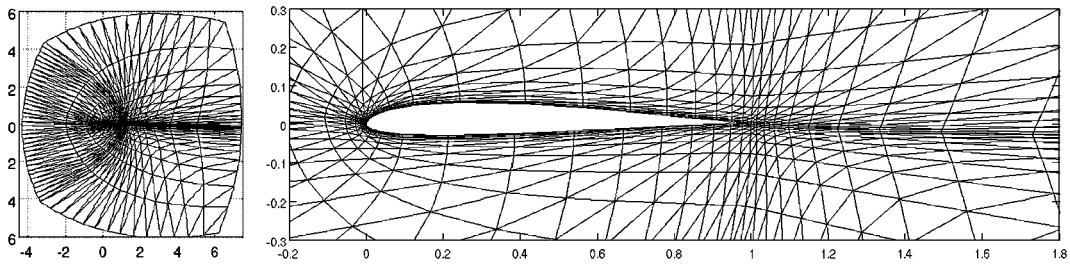

Figure 2. Span-wise plane of the coarse grid (grid 1): (left) domain, (right) closer view on foil; 21 504 tetrahedral elements and 430 080 high-order nodes at $p = 3$.

DOI: 10.1002/nme

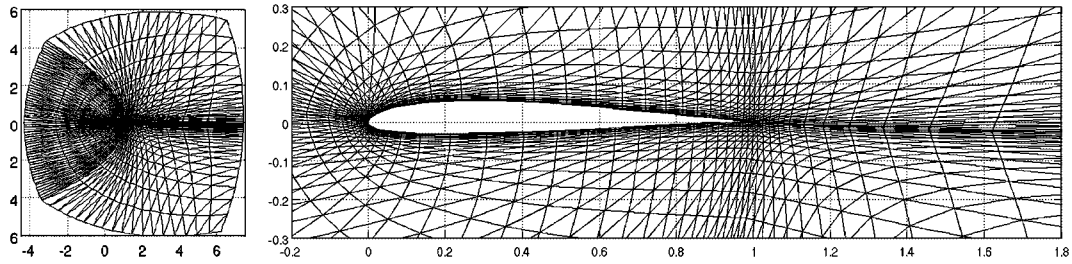

Figure 3. Span-wise plane of the medium grid (grid 2): (left) domain, (right) closer view on foil; 52 800 tetrahedral elements; 1 056 000 high-order nodes at $p=3$ and 1 848 000 nodes at $p=4$.

Table I. Characteristics of the computational grids employed.

Name	Number of elements	Polynomial order	Number of high-order nodes
Grid 1, $p=3$	21 504	3	430 080
Grid 2, $p=3$	52 800	3	1 056 000
Grid 2, $p=4$		4	1 848 000
Grid 3, $p=4$	85 500	4	2 992 500

Table I summarizes the spatial resolution characteristics of the different grids employed. For grid 1, third-order polynomials ($p=3$) are employed for a fourth-order accurate method in space, thus giving 430 080 high-order nodes. For grid 2, both third-order and fourth-order ($p=4$) polynomials are used, resulting in two refinement levels: one with 1 056 000 high-order nodes and the other one with 1 848 000. In the span-wise direction, both grids 1 and 2 have four elements, thus providing 13 and 17 unique nodes along the span at $p=3$ and $p=4$, respectively. Grid 3 has 15% more points than grid 2 in each direction (around the foil, radially, and along the span), and we use it with $p=4$ for a total of 2 992 500 high-order nodes. Note that the factor of 1.15 in grid spacing h corresponds to a factor of 2 in the convergence rate h^{p+1} of the DG method for smooth problems with $p=4$.

Throughout this paper, $p=3$ is used whenever no polynomial order is specified.

3.6. Angle of attack for XFOIL comparisons

XFOIL [36] is a two-dimensional, steady, potential flow solver with an interactive boundary layer coupling and an e^N envelope method for transition prediction [12]. It was developed for the design and analysis of subsonic airfoils, and has been extensively validated.

The Navier–Stokes methods apply the specified free-stream angle $\alpha=4^\circ$ at the domain's outer inflow boundary. The missing vortex upwash at the inlet due to the airfoil's presence gives a decrease in the effective angle of attack seen by the airfoil by the amount, in radians,

$$\Delta\alpha=-\frac{C_\mathrm{L}}{4\pi r/c},$$

where C_L is the airfoil lift coefficient and r/c is the distance-to-chord ratio between the inlet boundary and the wing's lift centroid such that the higher-order y-doublet far-field term is exactly zero. The distance between the airfoil's leading-edge and the center of lift can be approximated as

$$\frac{x_\mathrm{L}}{c}=\frac{1}{4}-\frac{C_\mathrm{M}}{C_\mathrm{L}},$$

which is a function of the moment coefficient C_M. The domain extends $4.3c$ upstream of the leading-edge, and hence $r/c=4.3+x_\mathrm{L}/c$. Note that the $\Delta\alpha$ correction is only significant when the domain inflow boundary is close to the foil as in the present work.

DOI: 10.1002/nme

Table II. Angle of attack correction, $\Delta\alpha$, and angle of attack for XFOIL computations, α_{XFOIL}, for the three Reynolds numbers considered.

Reynolds number	$C_{\mathrm{L}}(4^\circ)$	$C_{\mathrm{M}}(4^\circ)$	x_{L}/c	$\Delta\alpha$ ($^\circ$)	α_{XFOIL} ($^\circ$)
10 000	0.2842	−0.0167	0.3088	−0.2812	3.72
22 000	0.4083	−0.0466	0.3641	−0.3991	3.60
60 000	0.6370	−0.0347	0.3045	−0.6308	3.37

Since XFOIL fully accounts for the farfield vortex, it has been run at the smaller angle of attack $\alpha_{\mathrm{XFOIL}}=\alpha+\Delta\alpha$ in order to give a more correct comparison to the Navier–Stokes results. As an approximation, the lift and moment coefficients for computing $\Delta\alpha$ are obtained from XFOIL at the nominal 4° angle of attack. Table II gives the angle of attack correction and effective angle of attack for the different Reynolds numbers considered in the present work. Furthermore, the critical amplification factor in XFOIL is set to $N_{\mathrm{crit}}=7$.

3.7. Q-criterion

A way of identifying vortical coherent structures in a flow is to use the q-criterion proposed by Dubeif and Delcayre [37] and defined as

$$q \equiv \tfrac{1}{2}\left(\Omega_{ij}\Omega_{ij} - S_{ij}S_{ij}\right), \tag{9}$$

where Ω_{ij} and S_{ij} are the anti-symmetric and symmetric parts of the velocity gradient, respectively, that is

$$\Omega_{ij} \equiv \frac{1}{2}\left(\frac{\partial u_i}{\partial x_j} - \frac{\partial u_j}{\partial x_i}\right) \quad \text{and} \quad S_{ij} \equiv \frac{1}{2}\left(\frac{\partial u_i}{\partial x_j} + \frac{\partial u_j}{\partial x_i}\right).$$

For an incompressible fluid, the above can be written using the flow vorticity ω as

$$q = \frac{1}{4}\left(\omega^2 - 2S_{ij}S_{ij}\right) = \frac{1}{2}\frac{\nabla^2 p}{\rho}. \tag{10}$$

The q-criterion thus represents the balance between the rate of vorticity $\Omega^2=\Omega_{ij}\Omega_{ij}$ and the rate of strain $S^2=S_{ij}S_{ij}$. In the core of a vortex, $q>0$ since vorticity increases as the center of the vortex is approached. Thus, regions of positive q-criterion correspond to vortical structures. In the present work, iso-surfaces of positive q computed from (9) are used to visualize these structures.

3.8. Boundary layer parameters

In order to study the boundary layer, it is useful to consider the pseudo-velocity profile based on the flow vorticity $\vec{\omega}$ and defined by

$$\vec{u}^*(x,n) \equiv \int_0^n \vec{\omega}\times\hat{n}\,\mathrm{d}n. \tag{11}$$

Here $\hat{n}$ is the local unit vector that is normal to the wing's surface at the location considered, and n the local coordinate along the direction of $\hat{n}$, with the wall at $n=0$. The reason for using this pseudo-velocity profile is that it always asymptotes to a constant value outside the boundary layer where the vorticity becomes zero. This is so even in flows with strong curvature, thus making the edge of the boundary layer a well-defined quantity.

The edge, n_e, of the boundary layer is then taken to be the location where *both* the magnitudes of vorticity, $|\vec{\omega}|$, and of vorticity variation along the normal, $|\partial\vec{\omega}/\partial n|$, are below a certain threshold relative to the pseudo-velocity magnitude $|\vec{u}^*|$, namely

$$\begin{aligned} |\vec{\omega}|\,n &< \varepsilon_1|\vec{u}^*|, \\ \left|\frac{\partial\vec{\omega}}{\partial n}\right| n^2 &< \varepsilon_2|\vec{u}^*|. \end{aligned} \tag{12}$$

DOI: 10.1002/nme

The edge velocity is then $\vec{u}_e^* = \vec{u}^*(n_e)$, with magnitude $u_e = |\vec{u}_e^*|$. The values $\varepsilon_1 = 0.01$ and $\varepsilon_2 = 0.1$ were found to allow for a robust and systematic detection of the boundary layer edge for the simulations reported in the present work.

Local stream-wise and cross-flow unit vectors are defined as, respectively,

$$\hat{s}_1 \equiv \vec{u}_e / u_e \quad \text{and} \quad \hat{s}_2 \equiv \hat{s}_1 \times \hat{n}. \tag{13}$$

Thus, the stream-wise and cross-flow velocity profiles are, respectively, given by

$$u_1(x,n) = \vec{u}^*(x,n) \cdot \hat{s}_1 \quad \text{and} \quad u_2(x,n) = \vec{u}^*(x,n) \cdot \hat{s}_2. \tag{14}$$

The boundary layer stream-wise displacement and momentum thicknesses are then

$$\delta_1^* = \int_0^{n_e} \left(1 - \frac{u_1}{u_e}\right) \mathrm{d}n, \tag{15}$$

$$\theta_{11} = \int_0^{n_e} \left(1 - \frac{u_1}{u_e}\right) \frac{u_1}{u_e} \mathrm{d}n, \tag{16}$$

with the shape factor

$$H_{11} = \frac{\delta_1^*}{\theta_{11}}. \tag{17}$$

3.9. Transition mechanism

Since we want to identify which mechanism is responsible for transition to turbulence, we compute the fluctuating stream-wise pseudo-velocity

$$u_1'(\vec{x},t) = u_1(\vec{x},t) - \overline{u}_1(x),$$

where the overline denotes a temporal average. The increase in perturbation amplitude of disturbances along the chord-wise direction is then quantified by computing the amplification A_1 of stream-wise perturbations at any location x along the chord, that is

$$A_1(x) = \frac{1}{\overline{u_e}(x)\sqrt{n_e(x)}} \sqrt{\int_0^{n_e} \overline{u_1'^2}\, \mathrm{d}n}. \tag{18}$$

The amplification factor N_1 of the stream-wise perturbations is then

$$N_1(x) = \ln\left(\frac{A_1(x)}{A_{1_0}}\right), \tag{19}$$

in which A_{1_0} is the amplification at the onset of transition, or equivalently

$$e^{N_1} = \frac{A_1(x)}{A_{1_0}}.$$

4. LAMINAR REGIME: $Re = 10\,000$

The first case considered is the flow at a Reynolds number of 10 000 (Table III). In this regime, the flow is found to be fundamentally two-dimensional with little variation along the span-wise direction and periodic vortex shedding. Comparison is made with a two-dimensional simulation performed on a grid with the same resolution than a span-wise plane of the three-dimensional grid 2. While the instantaneous forces of Figure 4 differ slightly in magnitude, with slightly smaller amplitudes for the 3D case due to 3D alleviation, the shedding period and average values are essentially the same. The average lift coefficient is 0.3743, the average drag coefficient is 0.04967,

DOI: 10.1002/nme

Table III. Average flow results at Reynolds 10 000.

Source	Separation x_{sep}/c	Transition x_{tr}/c	Reattachment x_r/c	$\overline{C_L}$	$\overline{C_D}$
XFOIL at 3.72°, $N_{crit}=7$	0.3543	—	—	0.2711	0.04578
Grid 1	0.3658	0.9371	—	0.3824	0.04999
Difference with grid 2 (%)	2.8	−0.1	—	2.2	0.64
Grid 2, 2D	0.3451	0.9384	—	0.3755	0.04978
Difference with grid 2 (%)	−3.0	0	—	0.32	0.22
Grid 2	0.3557	0.9384	—	0.3743	0.04967
Difference with XFOIL (%)	0.39	—	—	38	8.5

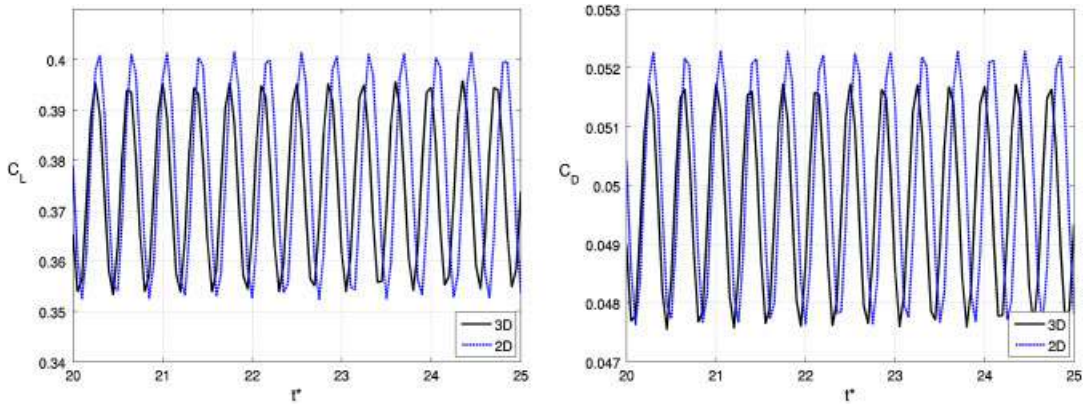

Figure 4. Time variation of lift (left) and drag (right) coefficients at $Re=10\,000$ on grid 2: comparison of 2D and 3D simulations.

whereas the average span-wise force coefficient is of the order of 10^{-6}. The difference in lift and drag coefficients of the two-dimensional simulation relative to the three-dimensional run is less than 0.32 and 0.23%, respectively. Furthermore, the 2D and 3D curves for average pressure and stream-wise skin friction coefficients are undistinguishable.

Note that the force coefficients are those of the time-averaged flow, and not exactly equal to the average of the force time variations; that is, the flow time average is computed first and then the forces of that time-averaged flow are evaluated. The difference in values between these two ways of obtaining force averages is usually insignificant (a couple of percents or less).

The effect of grid resolution is assessed by comparing the results obtained on grids 1 and 2. No significant difference is observed on average quantities, and the pressure and skin friction coefficient plots for the two grids fall on top of each other, whereas the average lift and drag coefficients for grid 1 differ by only 2.2 and 0.64%, respectively, from those for grid 2. On the other hand, there is a small but appreciable difference in the time history of the forces of Figure 5. Thus, grid 2 has sufficient resolution to capture the *mean* flow characteristics at $Re=10\,000$ although the time-varying features are not fully accounted for.

Furthermore, considering a spatial average over 10 span-wise planes instead of over 20 gives undistinguishable pressure and skin friction curves at this Reynolds number. The same is true when averages are computed over 100 solutions instead of over 200. The statistics obtained with 200 solutions and 20 span-wise planes at this regime are thus properly converged.

Figures 6 shows the average pressure and stream-wise skin friction coefficients, together with the results predicted by XFOIL [36] at an angle of attack of 3.72° as justified in Section 3.6. The similarity with XFOIL provides a good check for the present simulations, but the two approaches may not correspond to precisely the same far-field conditions. First, the angle of attack correction is only an approximation. Furthermore, the critical amplification factor, N_{crit}, at which transition is set

DOI: 10.1002/nme

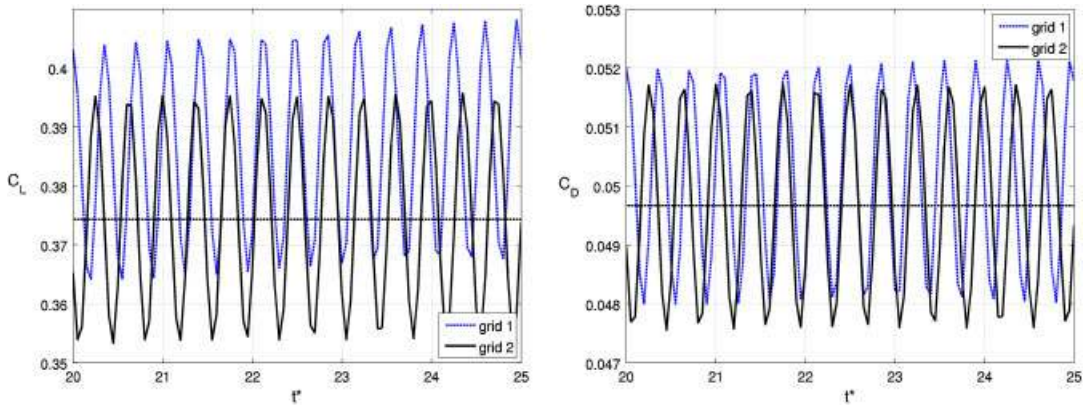

Figure 5. Time variation of lift (left) and drag (right) coefficients at $Re = 10000$: comparison between grids 1 and 2. The dotted horizontal line indicates the average value for grid 2.

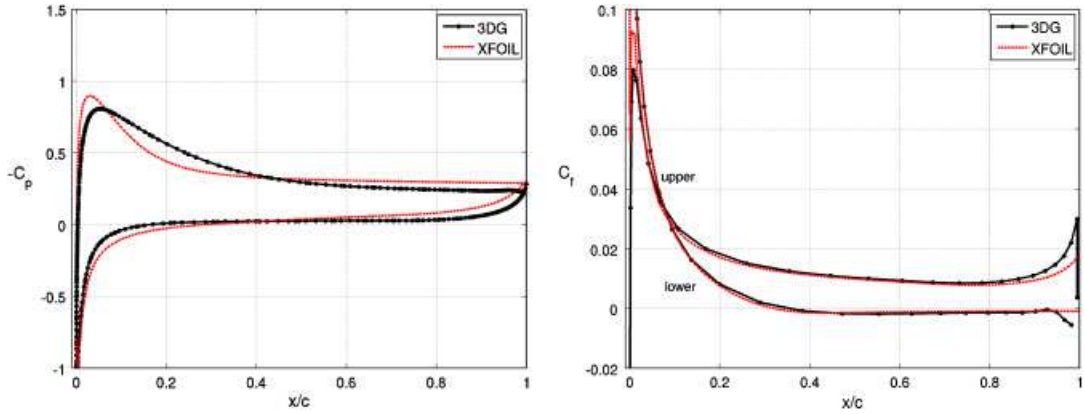

Figure 6. Average pressure coefficient (left) and stream-wise skin friction coefficient (right) at $Re = 10000$ on grid 2. The dashed lines give XFOIL predictions at 3.72° angle of attack, $N_{\text{crit}} = 7$.

to occur (a user-defined parameter in XFOIL) is correlated to the level of free-stream disturbances, and it is unclear what the value for a simulation should be. In the present case, setting N_{crit} to 4.6 in XFOIL results in a match in transition location.

The iso-surfaces of q-criterion of Figure 8 show that coherent vortical structures are not present upstream of the trailing edge but only in the wake. Furthermore, the instantaneous iso-surfaces have a straight cylindrical shape with no variation along the span-wise direction, thus indicating that the wake structures remain two-dimensional.

At this Reynolds number, the boundary layer separates at around 36% of the chord from the leading-edge, and does not reattach. This can be seen on the friction coefficient distribution of Figure 6, on the instantaneous and average span-wise vorticity contours as shown in Figure 7, and on the average streamlines shown in Figure 9. Furthermore, the flow structures are all relatively large with only pairs of well-defined vortices being shed (see Figure 7).

The curves of stream-wise displacement thickness, δ_1^*, momentum thickness, θ_{11}, and shape factor, $H_{11} = \delta_1^*/\theta_{11}$, of Figure 10 confirm that transition to turbulence occurs only at 94% of the chord. Furthermore, the curves for two-dimensional simulations and for grid 1 are undistinguishable from those of grid 2. The main difference between the boundary layer evolution as predicted by XFOIL (dashed lines in the figures) and the one resulting from the present ILES is that the latter predicts a transition to turbulence just upstream of the trailing edge as evidenced by the peak in shape factor, whereas the former does not.

DOI: 10.1002/nme

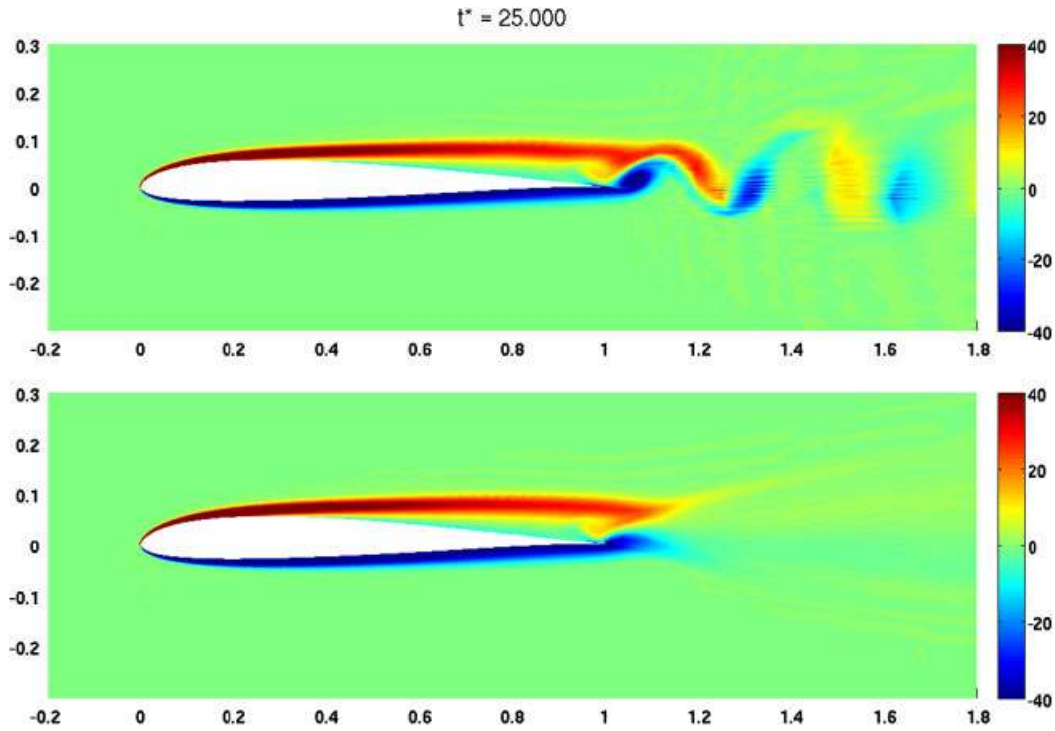

Figure 7. Span-wise vorticity at $Re = 10000$ with grid 2: instantaneous span-wise average (top) and average (bottom) contours.

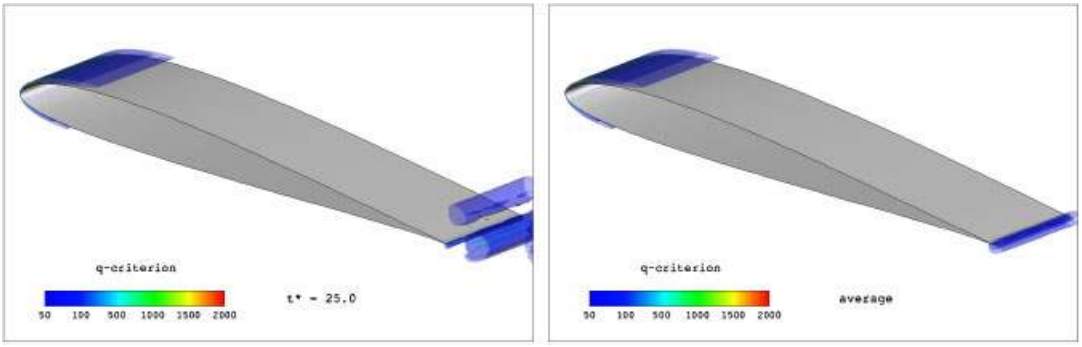

Figure 8. Instantaneous (left) and time average (right) iso-surfaces of q-criterion at $Re = 10000$ with grid 2.

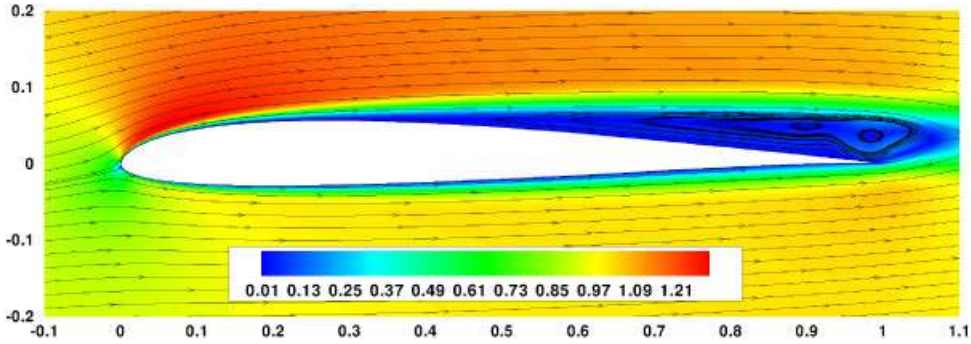

Figure 9. Average steamlines at $Re = 10000$ with grid 2, and contours of velocity magnitude.

DOI: 10.1002/nme

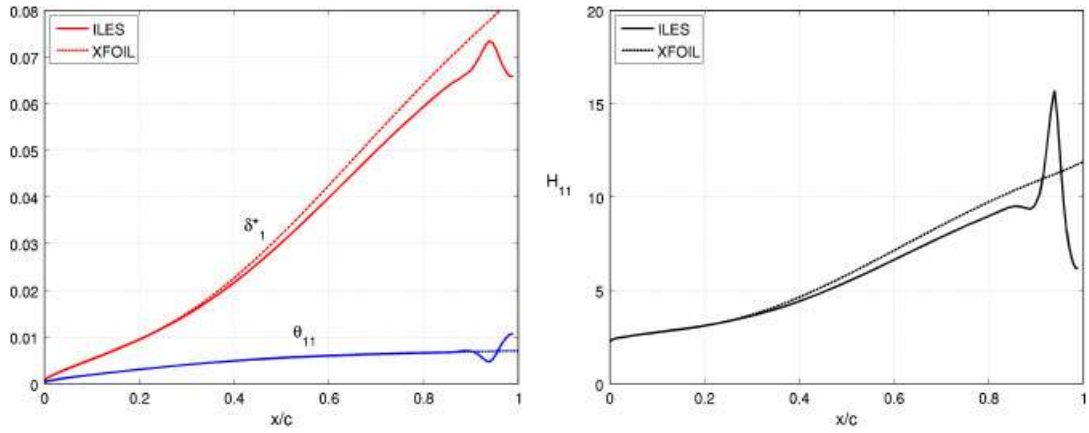

Figure 10. Boundary layer average stream-wise displacement and momentum thicknesses (left), and shape factor (right) evolution along the chord-wise direction at $Re=10\,000$ with grid 2. The dashed lines give XFOIL predictions at 3.72° angle of attack, $N_{\text{crit}}=7$.

5. LOW TRANSITIONAL REGIME: $Re=22\,000$

Next a flow at a Reynolds number of 22 000 is considered. As previously, the three-dimensionality and the effects of grid resolution are studied.

5.1. Three-dimensionality

The flow at this Reynolds number transitions to turbulence, and since turbulence is a fundamentally three-dimensional phenomena, we expect that a two-dimensional simulation would not be able to capture the important flow features. This is confirmed by comparing the three-dimensional results obtained on grid 2 with a two-dimensional simulation using, as previously, a grid with the same resolution as a span-wise plane.

With respect to the instantaneous force coefficients of Figure 11, it can be noted that the lift and drag force coefficients for the two-dimensional case have significantly larger magnitudes (by close to a factor of three) than those of the three-dimensional case. This is of course due to three-dimensional alleviating effects.

The pressure and skin friction profiles of Figure 12 also confirm the significance of three-dimensional effects, with the friction being more sensitive than the pressure, whereas the largest discrepancies occur near transition ($x/c\approx 0.7$). However, a two-dimensional flow approximation yields separation, transition, and reattachment locations, as well as lift and drag coefficients, which are relatively close (less than 10% off) to the three-dimensional solution values as indicated by the numbers in Table IV.

5.2. Spatial resolution: grid comparisons

In order to assess how much spatial resolution is needed at $Re=22\,000$, the flow is computed on three different resolution levels: grid 1 with $p=3$, grid 2 with $p=3$, and grid 2 with $p=4$. The curves of average pressure coefficient and average skin friction coefficient profiles for the three levels are undistinguishable; the common profiles can be seen, for instance, in Figure 12. On the other hand, the instantaneous force histories of Figure 13 differ but have approximately the same magnitudes. They depict a turbulent signal and indicate an a-periodic vortex shedding with various scale sizes and frequencies. Furthermore, the span-wise force coefficient, while small (of the order of 10^{-4}), reveals the presence of span-wise flow motions. The average separation, transition, and reattachment locations, as well as the lift and drag coefficients of the mean flow are given in Table IV. The separation location has a relatively large uncertainty (C_{f} curve is flat there) so the 6.6% difference between grid 2, $p=3$ and $p=4$ is not significant.

DOI: 10.1002/nme

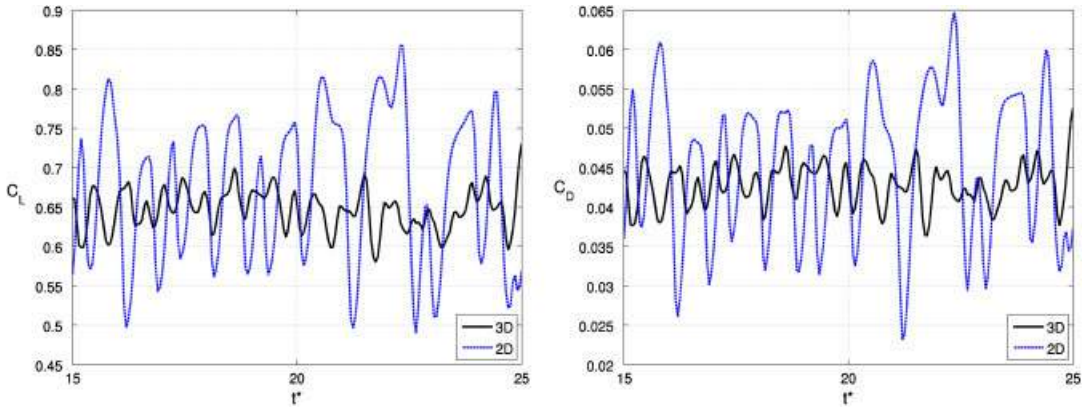

Figure 11. Time variation of lift (left) and drag (right) coefficients at $Re = 22\,000$ on grid 2: comparison of 2D and 3D simulations.

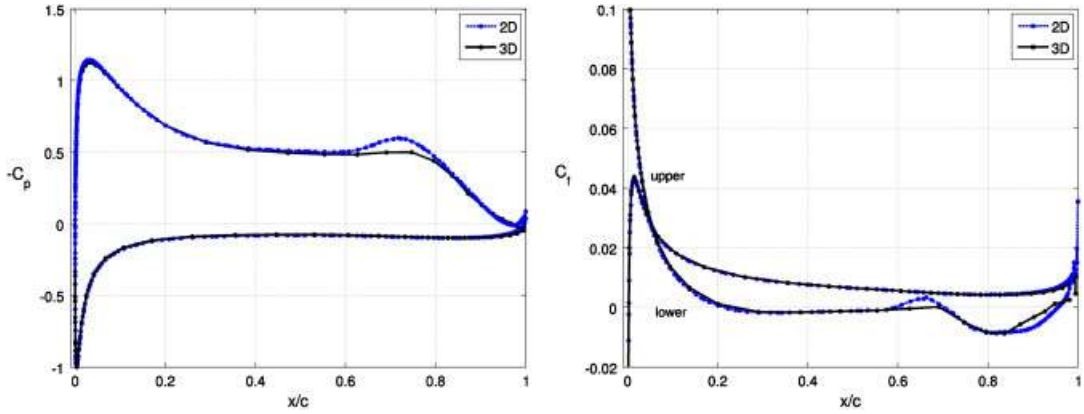

Figure 12. Average pressure coefficient (left) and stream-wise skin friction coefficient (right) at $Re = 22\,000$ on grid 2: comparison of 2D and 3D simulations.

Table IV. Average flow results at Reynolds 22 000.

Source	Separation x_{sep}/c	Transition x_{tr}/c	Reattachment x_r/c	Bubble length	$\overline{C_L}$	$\overline{C_D}$
XFOIL at 3.60°, $N_{crit} = 7$	0.2489	0.7784	0.9494	$0.7005c$	0.5193	0.03772
Grid 1	0.2744	0.6853	—	—	0.6359	0.04309
Difference with grid 2 (%)	15	0.60			−1.5	0.87
Grid 2, 2D	0.2144	0.6602	0.9554	$0.7410c$	0.6707	0.04510
Difference with grid 2 (%)	−10	−3.1	1.9	6.0	3.9	5.6
Grid 2	0.2386	0.6812	0.9379	$0.6993c$	0.6456	0.04272
Difference with grid 2, $p = 4$ (%)	6.6	0.95	0.011	−2.0	−0.031	−0.37
Grid 2, $p = 4$	0.2239	0.6748	0.9378	$0.7139c$	0.6458	0.04288
Difference with XFOIL (%)	−10	−13	−1.2	1.9	24	14

Furthermore, the boundary layer chord-wise variation of stream-wise displacement thickness and momentum thickness are not significantly different. On the other hand, the shape factor does show a discrepancy but only in the separation region ($H_{11} > 4$) and not in the transition location as can be seen in Figure 14. Thus, the results obtained on grid 2 with $p = 3$ can be considered to be grid-converged with respect to global average quantities, and this mesh is characteristic of the spatial resolution needed to resolve the mean flow features at $Re = 22\,000$.

DOI: 10.1002/nme

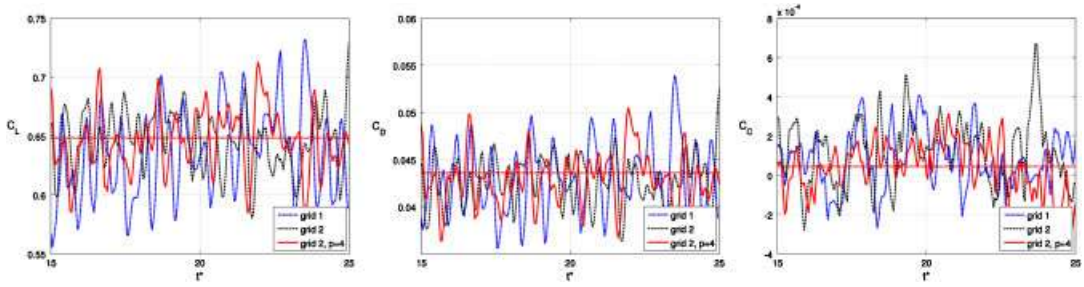

Figure 13. Time variation of lift (left), drag (center), and span-wise (right) force coefficients at $Re = 22\,000$: comparison of results with different spatial resolutions. The dotted horizontal line indicates the average value for grid 2, $p = 4$.

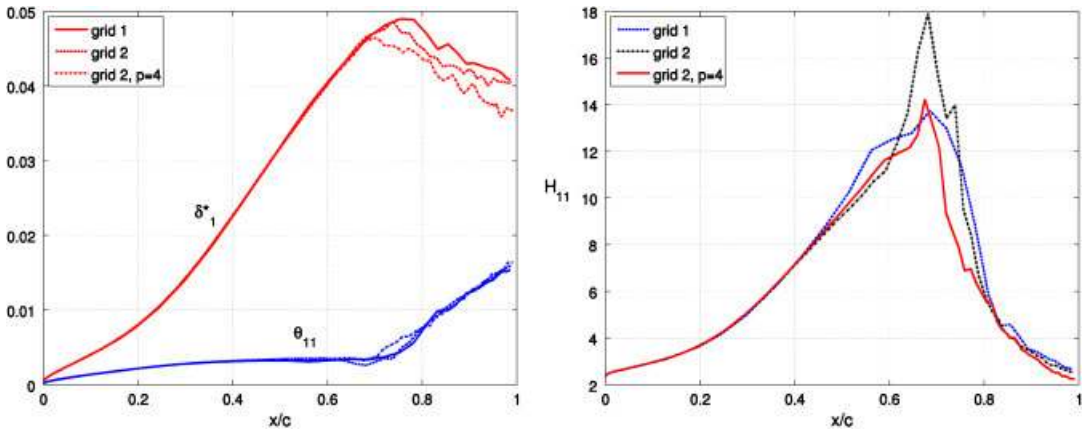

Figure 14. Boundary layer average stream-wise displacement and momentum thicknesses (left), and shape factor (right) evolution along the chord-wise direction at $Re = 22\,000$: comparison of results with different spatial resolutions.

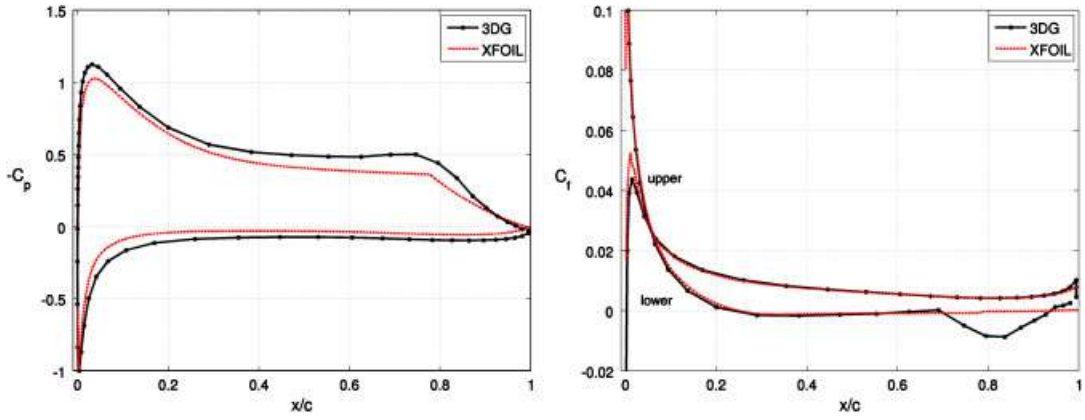

Figure 15. Average pressure coefficient (left) and stream-wise skin friction coefficient (right) at $Re = 22\,000$ on grid 2. The dashed lines give XFOIL predictions at 3.60° angle of attack, $N_{\text{crit}} = 7$.

5.3. Results with grid 2, $p = 3$

At this Reynolds number of 22 000, the separation bubble is clearly visible on the C_p profile of Figure 15 with the characteristic plateau. From the skin friction coefficient, separation is located at around 23% of the chord. Transition takes place after separation, at around 68% as measured from the peak in the boundary layer shape factor of Figure 20; this is also made visible by the velocity

DOI: 10.1002/nme

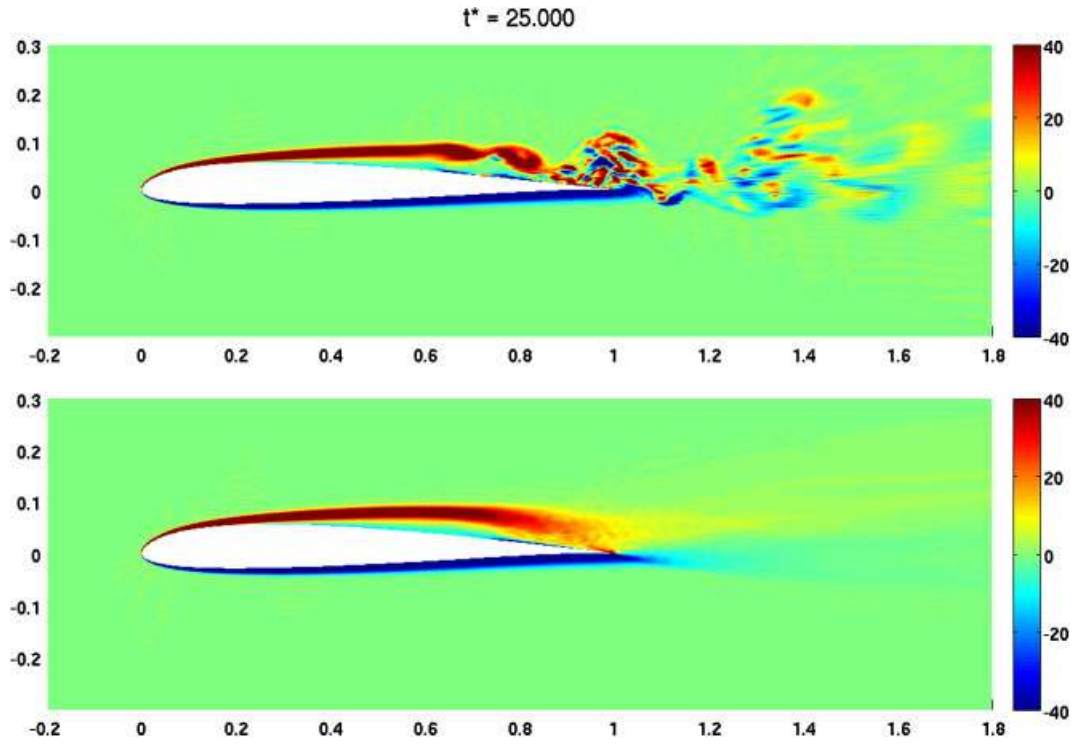

Figure 16. Span-wise vorticity at $Re = 22\,000$ with grid 3, $p = 4$: instantaneous span-wise average (top) and average (bottom) contours.

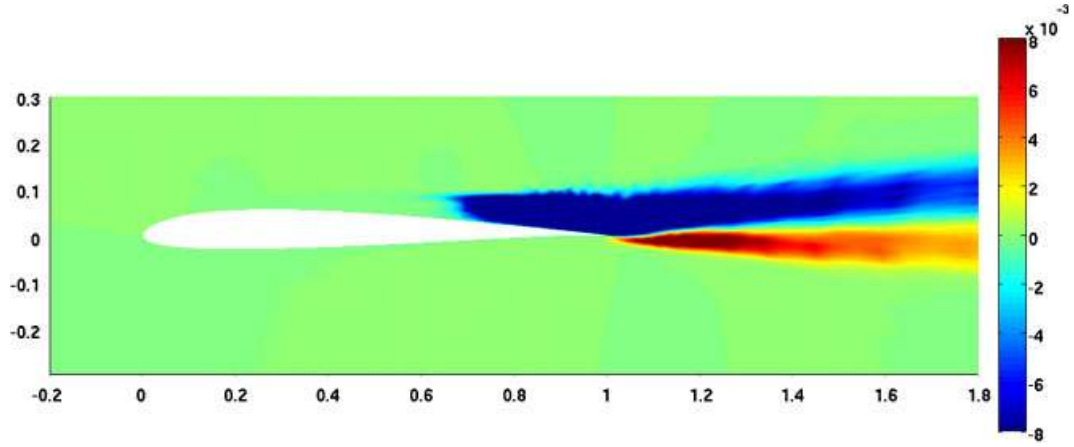

Figure 17. Non-dimensional streamwise-transverse velocity correlations $\overline{u'_s u'_t}/U_\infty^2$ at $Re = 22\,000$ with grid 3, $p = 4$.

correlations of Figure 17, which show significant velocity fluctuations on the downstream part of the foil. Finally, the flow reattaches at around 94% of the chord, thus forming a long separation bubble that encompasses more than 70% of the wing's chord. This LSB is made visible by the average streamlines of Figure 19.

Contrarily to what was observed at $Re = 10\,000$, the instantaneous vorticity contours of Figure 16 contain a significant amount of small, high-frequency structures, and the flow is not anymore restricted to pairs of shed vortices. As already pointed out, the flow at this Reynolds number is three-dimensional and contains structures that vary in the span-wise direction. This can be

DOI: 10.1002/nme

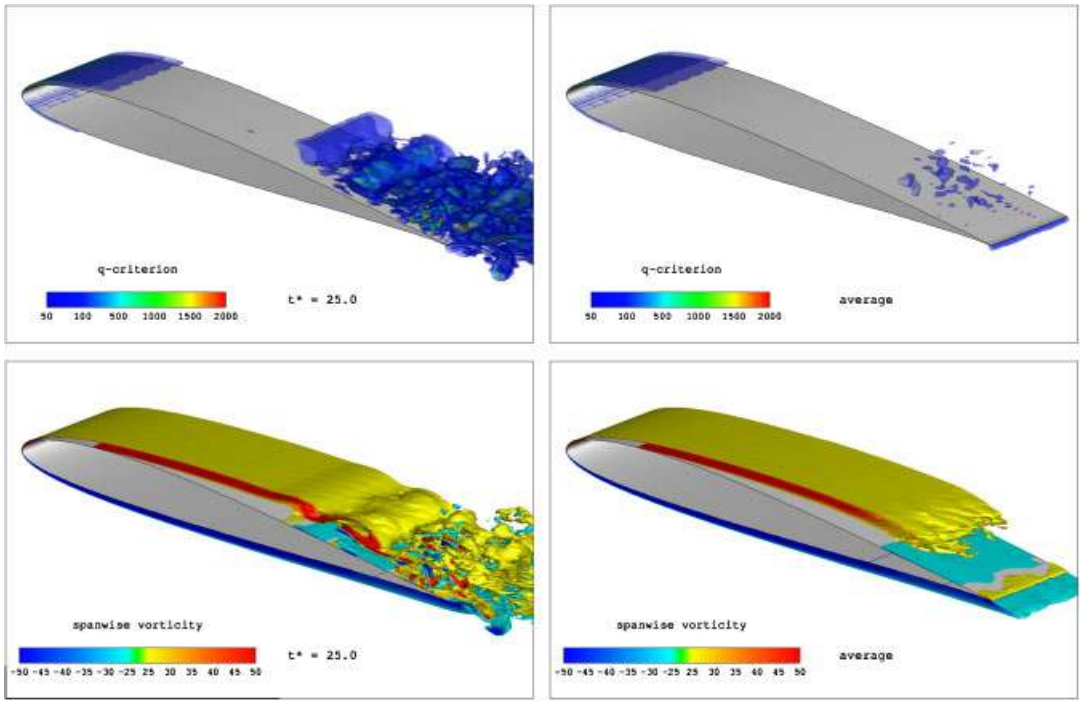

Figure 18. Instantaneous (left) and average (right) iso-surfaces of q-criterion (top) and span-wise vorticity (bottom) at $Re = 22\,000$ with grid 3, $p = 4$.

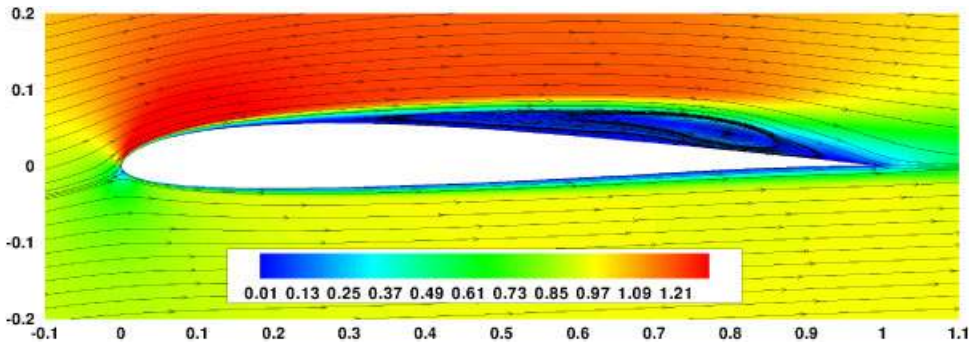

Figure 19. Average steamlines at $Re = 22\,000$ with grid 3, $p = 4$ and contours of velocity magnitude.

seen in the instantaneous iso-surfaces of q-criterion and of span-wise vorticity of Figure 18: the iso-surfaces are not cylindrical and reveal significant span-wise variations.

The comparison with XFOIL's predictions show some disagreement—see the pressure and friction profiles of Figure 15 and the boundary layer integral thickness evolutions of Figure 20—but the same remarks made for the $Re = 10\,000$ case hold here, and the comparisons provide merely a consistency check. Transition, for instance, can be made to match by setting a critical amplification factor of $N_{\text{crit}} = 5.2$ in XFOIL. Furthermore, the flow at this Reynolds number is three-dimensional and is beyond the modeling capabilities of XFOIL.

5.4. Transition mechanism

A close look at the boundary layer of the average flow provides insight into the transition process. From the shape factor of Figure 20, the transition location is clearly identified by the peak, whereas the separated flow can be identified as the region where H_{11} is larger than 4. The left

DOI: 10.1002/nme

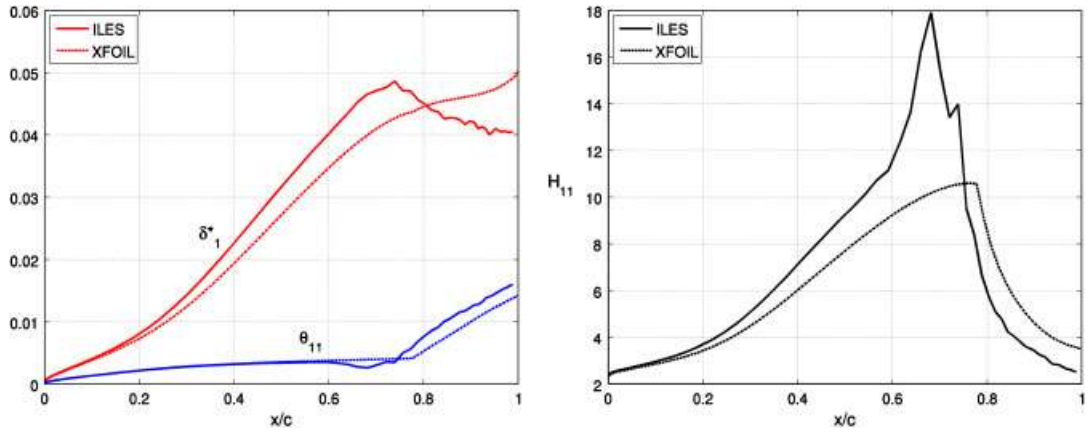

Figure 20. Boundary layer average stream-wise displacement and momentum thicknesses (left), and shape factor (right) evolution along the chord-wise direction at $Re=22\,000$ with grid 2. The dashed lines give XFOIL predictions at 3.60° angle of attack, $N_{\text{crit}}=7$.

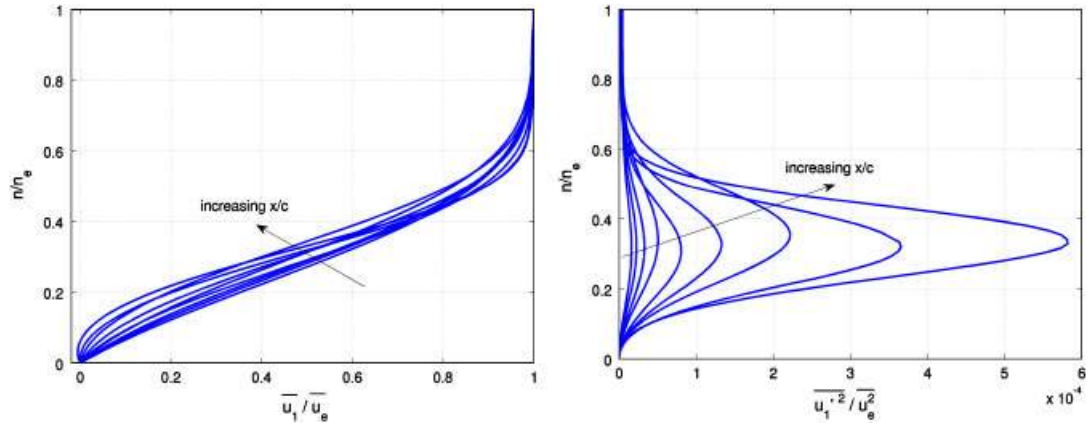

Figure 21. Boundary layer average profiles of stream-wise pseudo-velocity $\overline{u}_1/\overline{u_e}$ (left) and fluctuating stream-wise pseudo-velocity $\overline{u_1'^2}/\overline{u_e^2}$ (right), at different chord-wise locations $x/c\in[0.1, 0.3]$ at $Re=22\,000$ with grid 2.

plot of Figure 21 shows average profiles of stream-wise pseudo-velocity at several chord-wise locations $x/c\in[0.1, 0.3]$, which resemble the profiles over a flat plate by the construction of the pseudo-velocity through Equation (11).

As explained in Section 3.9, the transition mechanism can be determined by considering the profiles of fluctuating stream-wise pseudo-velocity, $\overline{u_1'^2}/\overline{u_e^2}$, of Figure 21. Each profile's shape is consistent with the superposition of TS waves whose amplitude increases along the chord-wise direction. Note also that the maximum moves away from the wall as it is convected downstream. The amplitude increase is quantified through the stream-wise amplification factor N_1 of Figure 38. This analysis clearly proves that transition is the result of the growth of TS waves, and hence that we are in the presence of a natural transition—not a bypass transition.

The chord-wise transition location determined previously from the shape factor ($x_{\text{tr}}/c=0.68$) can be used to observe that, according to the $N_1(x/c)$ curve, transition takes place at a critical amplification of $N_1=4.6$. This is close to the value of 5.2 required for XFOIL at 3.60° angle of attack to give agreement with respect to the transition location.

Note that the fluctuations observed in N_1 for $x/c>0.5$ indicate that temporal average needs to be carried out over a larger number of time steps due to separation and transition, this lack

DOI: 10.1002/nme

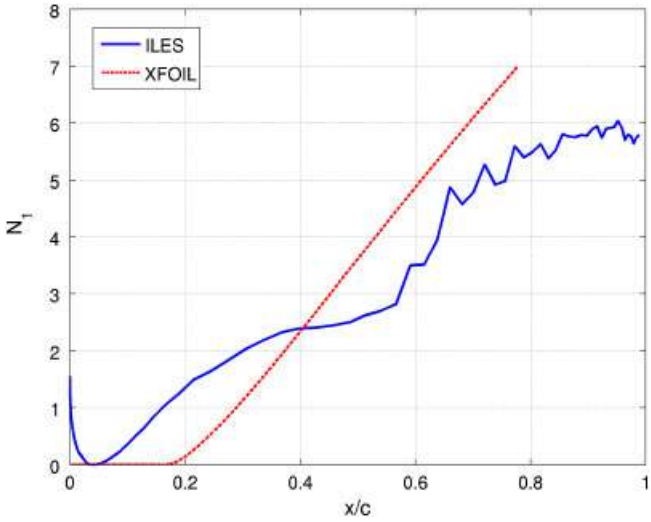

Figure 22. Amplification factor N_1 of stream-wise pseudo-velocity perturbations for the flow at $Re=22\,000$ with grid 2.

of statistical convergence being only evident for boundary layer considerations and hence only observed in Figures 20 and 22.

6. HIGH TRANSITIONAL REGIME: $Re=60\,000$

As mentioned in the background section, the flow around the SD7003 at 4° angle of attack and Reynolds number of 60 000 has been studied by several groups. This case is considered in detail here, in particular the three-dimensional effects, the required resolution for ILES with DG, and the influence of span length and of time step. The transition mechanism is also established.

6.1. Three-dimensionality

As expected, at $Re=60\,000$ the flow cannot be approximated by a two-dimensional simulation. The magnitude of forces in Figure 23 from a two-dimensional simulation is about a factor of 9 times larger than the three-dimensional results: three-dimensional alleviation is even more significant than at $Re=22\,000$. Furthermore, while at a Reynolds number of 22 000 a two-dimensional simulation was able to capture the separation bubble, at $Re=60\,000$ no bubble is present in two-dimensional runs as made evident in the pressure and skin friction profiles of Figure 24: there is no plateau in average C_p but only a close to linear pressure rise along most of the upper surface (Table V).

6.2. Spatial resolution: grid comparisons

The required spatial resolution is assessed by comparing the results with several grids. We use grids 1 and 2 with polynomials of order 3 ($p=3$), as well as grids 2 and 3 with $p=4$. The distance between the wall and the first high-order node along the upper surface of the foil on grid 2, $p=3$, is approximately $\Delta y\approx 4\times 10^{-4}c$. At $x/c=0.1$ where $C_f\approx 0.01$, this corresponds to approximately $\Delta y^+\approx 2$ wall units, with the usual definition $y^+=u_\tau y/\nu$ for $u_\tau=\sqrt{\tau_w/\rho}=\sqrt{C_f/2}U_\infty$.

The comparison of force histories and of average pressure and skin friction coefficients on the airfoil obtained with the different spatial resolution levels can be seen in Figures 25 and 26. Grid 1 is unable to properly capture the separation bubble and associated transition to turbulence, giving only a short LSB and forces that are too small. With $p=3$, grid 2 provides a relatively accurate average flow but forces that are still too low, a delayed separation, and too rapid transition thus resulting again in an under-predicted bubble length. Finally, the magnitude of the temporal

DOI: 10.1002/nme

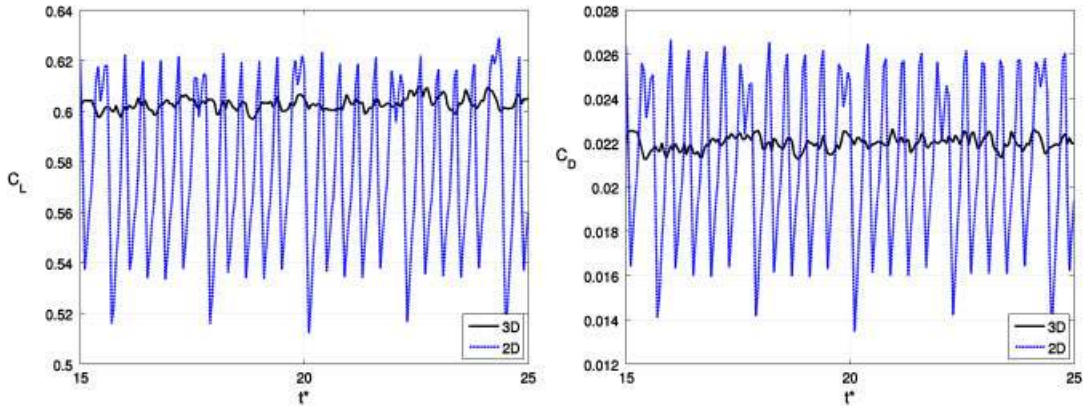

Figure 23. Time variation of lift (left) and drag (right) coefficients at $Re = 60\,000$ on grid 2: comparison of 2D and 3D simulations.

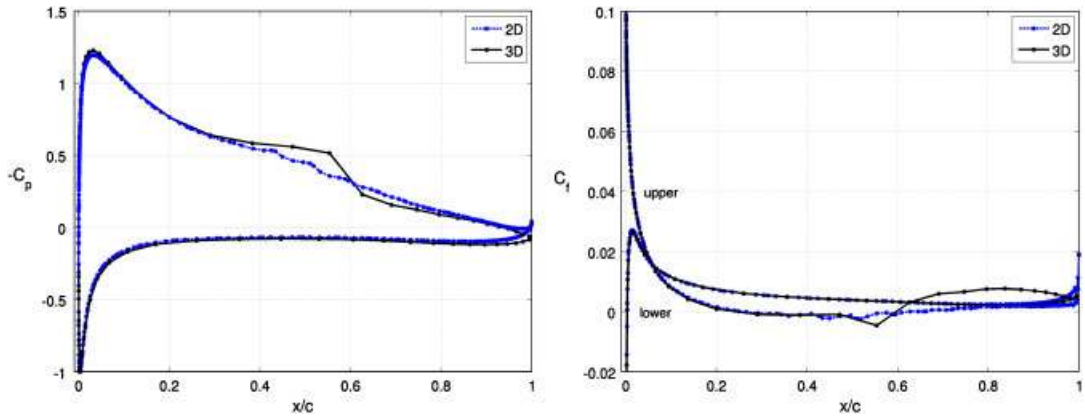

Figure 24. Average pressure coefficient (left) and stream-wise skin friction coefficient (right) at $Re = 60\,000$ on grid 2: comparison of 2D and 3D simulations.

Table V. Average flow results at Reynolds 60 000.

Source	Separation x_{sep}/c	Transition x_{tr}/c	Reattachment x_r/c	Bubble length	$\overline{C_L}$	$\overline{C_D}$
Grid 1	0.2907	0.4119	0.5396	0.2489c	0.5997	0.02058
Difference with grid 2 (%)	19	−20	−9.6	29	0.51	−6.4
Grid 2, 2D	0.2589	0.4295	0.6213	0.3624c	0.5730	0.02097
Difference with grid 2 (%)	6.1	−16.5	4.1	2.7	−4.9	−4.6
Grid 2	0.2440	0.5145	0.5967	0.3527c	0.6028	0.02198
Difference with grid 2, $p=4$ (%)	18	−3.6	−10	−23	−1.5	−8.7
Grid 2, span 0.3c	0.2306	0.5146	0.6233	0.3927c	0.6021	0.02196
Difference with grid 2 (%)	−5.5	0.019	4.5	11	−0.12	−0.091
Grid 2, Δt_1^*	0.2424	0.5146	0.6124	0.3700c	0.6033	0.02200
Difference with grid 2 (%)	−0.66	0.019	2.6	4.9	0.083	0.091
Grid 2, $p=4$, 2D	0.2544	0.4930	0.5811	0.3267c	0.5458	0.02142
Difference with grid 2, $p=4$ (%)	23	−7.6	−13	−29	−11	−11
Grid 2, $p=4$	0.2069	0.5335	0.6658	0.4589c	0.6122	0.02407
Difference with grid 3, $p=4$ (%)	−0.34	−1.1	−0.48	−0.54	0.39	0.042
Grid 3, $p=4$	0.2076	0.5397	0.6690	0.4614c	0.6098	0.02406

DOI: 10.1002/nme

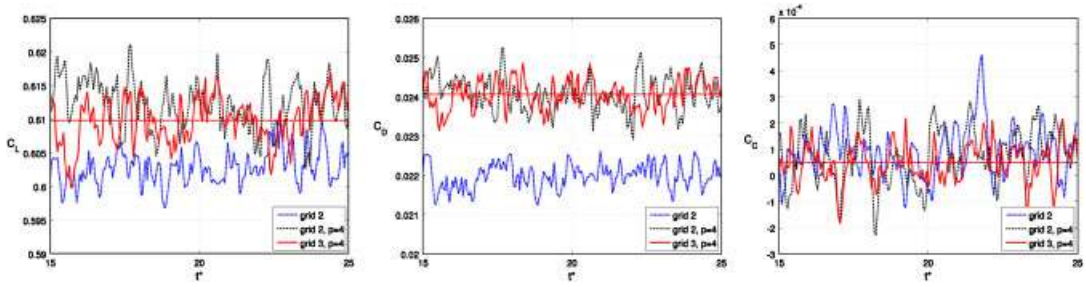

Figure 25. Time variation of lift (left), drag (center), and span-wise (right) force coefficients at $Re = 60\,000$: comparison of results with different spatial resolutions. The dotted horizontal line indicates the average value for grid 3, $p = 4$.

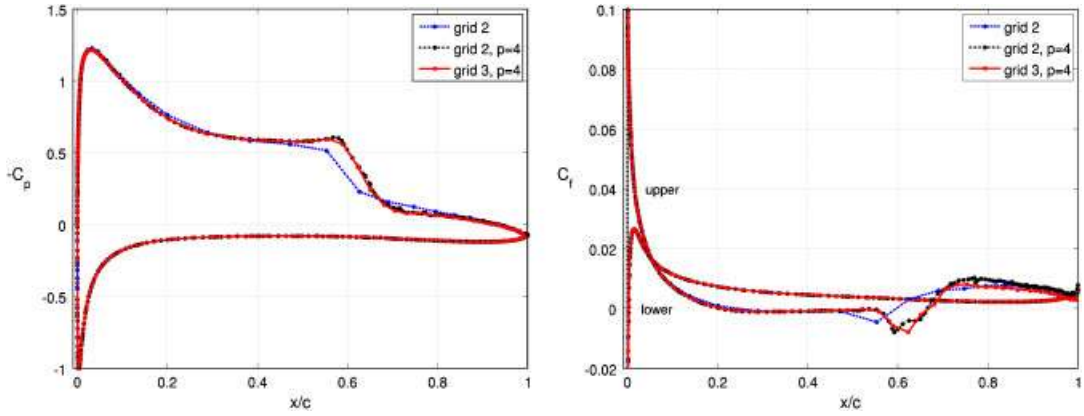

Figure 26. Average pressure coefficient (left) and stream-wise skin friction coefficient (right) at $Re = 60\,000$: comparison of results with different spatial resolutions.

evolution of forces, the average flow, and boundary layer integral thicknesses obtained on grid 2 with $p = 4$ and on grid 3 with $p = 4$ agree. Thus, grid 2 is able to provide the required spatial resolution when polynomials of order $p = 4$ are employed.

6.3. Effect of domain span length

In order to investigate what domain span length is required to simulate an infinite wing with a span-wise periodic boundary condition while properly capturing all the mean flow structures, a domain with a span of 0.3 chords was considered in addition to the 0.2 span used in all other simulations, with a grid identical to grid 2, $p = 3$, except in the span-wise direction. To preserve the span-wise resolution, $\frac{3}{2}$ times more nodes are used along the span: thus, this grid has six elements in the span-wise direction for 19 unique high-order nodes along the span, while grid 2 has four elements and 13 unique nodes span-wise. In this way, we ensure that comparing results with those on grid 2 reveals the effect of span length only, and is not related to resolution.

The time evolution of forces of Figure 27 show similar amplitudes and shapes for the two spans considered, although the exact curves do not overlap, as expected for a turbulent flow and just as is observed when comparing different grids. Furthermore, the curves of average pressure coefficient and skin friction coefficient profiles are undistinguishable between the two span lengths considered. However, small differences are observed in the boundary layer profiles as can be seen in Figure 28, but the separation, transition, and reattachment locations are essentially unchanged. A domain span of $0.2c$ is thus appropriate to capture the main flow features in the simulation of an infinite wing as observed by Galbraith and Visbal [3].

DOI: 10.1002/nme

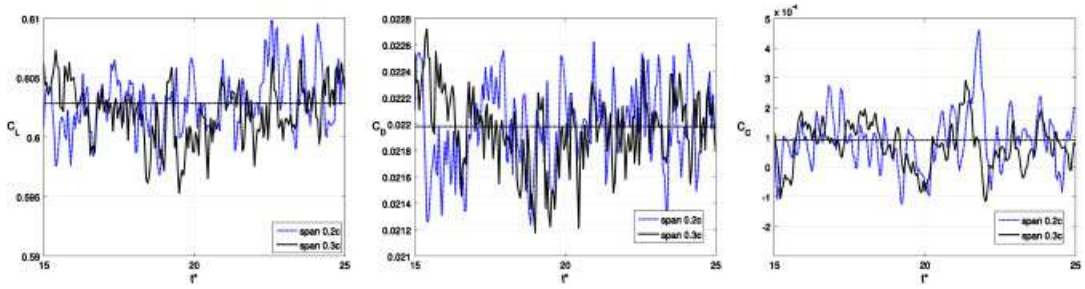

Figure 27. Time variation of lift (left), drag (center), and span-wise (right) force coefficients at $Re = 60\,000$ on grid 2: comparison of grids with two different span lengths.

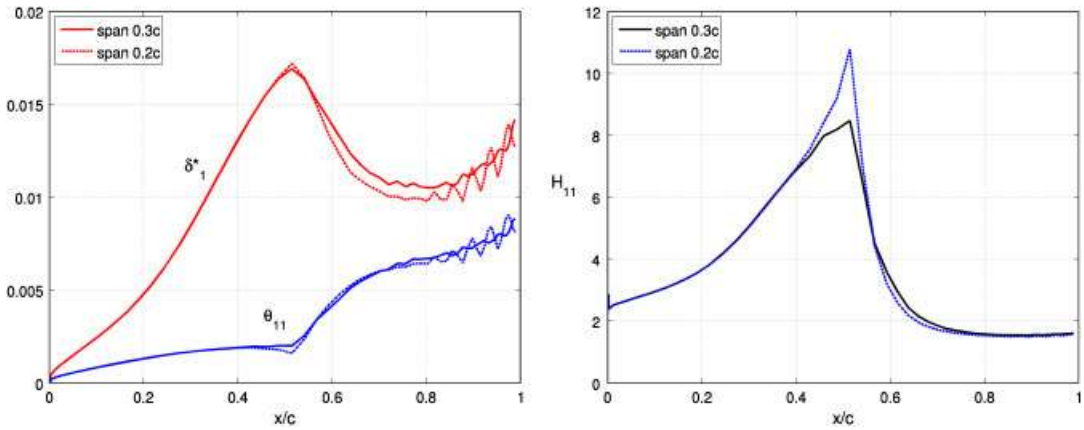

Figure 28. Boundary layer average stream-wise displacement and momentum thicknesses (left), and shape factor (right) evolution along the chord-wise direction at $Re = 60\,000$ with grid 2: comparison of grids with two different span lengths.

6.4. *Temporal resolution*

The use of an implicit time stepping procedure allows for the choice of large time steps irrespective of stability considerations. However, one should still ensure that the time resolution is sufficient to obtain accurate average quantities—although the instantaneous fields are of course dependent on the particular time resolution to capture certain frequencies.

A simulation on grid 2 with solutions saved every $\Delta t_1^* = 0.02$ is performed in order to assess whether the chosen value of $\Delta t_0^* = 0.05$ can appropriately capture the mean flow features. Note that the actual time step in the DIRK time stepping method is set to $dt^* = 0.01$ for both, but the solutions are saved either every five or every two steps for Δt_0^* and Δt_1^*, respectively. Note also that we have not chosen a multiple of the original time step Δt_0^* in order to avoid any possible sub-harmonic locking. When using the smaller time step Δt_1^*, statistics are computed over 500 steps (whereas 200 steps are used for Δt_0^*) in order to span the same time $t^* \in [15, 25]$; this also provides for a sense of the degree of convergence of the time-averaged fields and fluctuating quantities, which are now determined based on more steps.

As expected, the average pressure and friction profiles are not sensitive to the temporal resolution change, and the curves of $C_p(x/c)$ and $C_f(x/c)$ overlap. Furthermore, while the boundary layer thicknesses and shape factor evolution do not perfectly match between the runs at the two time steps, they are however very close and the time history of forces are similar (Figure 30). As can be seen in Figure 29, the shape factor curves are almost identical (maximum difference of 5% at transition), and the displacement and momentum thicknesses do overlap before transition with a maximum difference of 18 and 21% for displacement and momentum, respectively.

DOI: 10.1002/nme

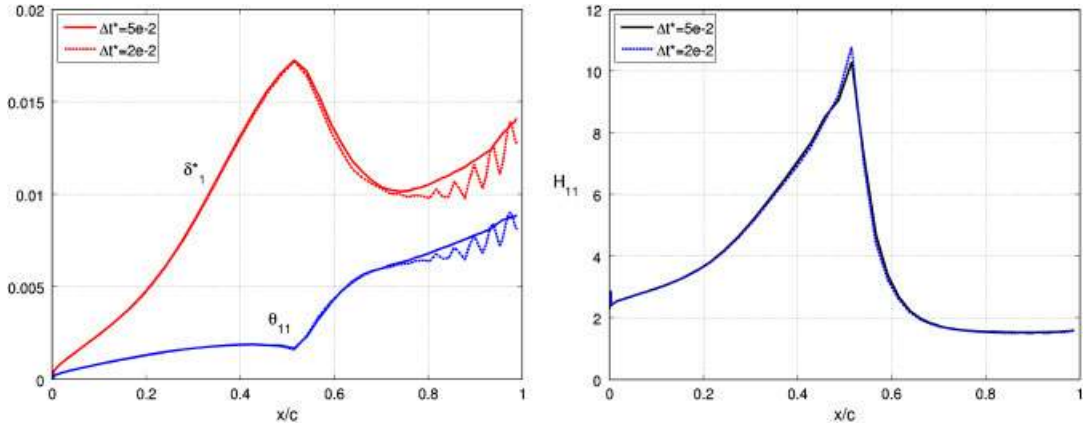

Figure 29. Boundary layer average stream-wise displacement and momentum thicknesses (left), and shape factor (right) evolution along the chord-wise direction at $Re=60000$ with grid 2: comparison for simulations saved every five time steps ($\Delta t^*=0.05$) and every two time steps ($\Delta t^*=0.02$). The time averages are carried out over 200 and over 500 instantaneous solutions, respectively.

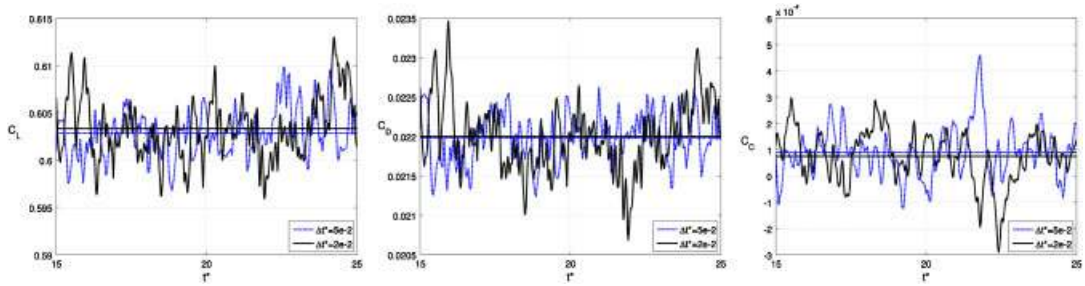

Figure 30. Time variation of lift (left), drag (center), and span-wise (right) force coefficients at $Re=60000$ on grid 2: comparison of simulations saved every five time steps ($\Delta t_0^*=0.05$) and every two time steps ($\Delta t_1^*=0.02$).

In spite of this, separation, transition, and reattachment locations are unaffected. Thus, we deem the temporal resolution of $\Delta t_0^*=0.05$ sufficient with respect to average statistics, although the small (high-frequency) structures in the boundary layer would require more resolution to be fully accounted for.

6.5. *Effect of averaging*

In order to verify that turbulence statistics are properly converged, we compared the results obtained by performing averages over 100 time steps (instantaneous solutions) and over 200 steps. The average pressure and skin friction coefficients over the wing are undistinguishable, whereas there is a small difference in boundary layer thicknesses and shape factor, comparable to that observed in Figure 29 when considering different temporal resolutions.

As mentioned in the methodology section, the average quantities are obtained by computing a time average followed by a spatial span-wise average. For the latter, the solution is first interpolated (to an order compatible with the polynomial order being used so as to avoid interpolation errors) at 20 different planes perpendicular to the span-wise direction, and these 20 interpolated solutions are then averaged. The use of only 10 planes was tested and again provided results that compared with the use of 20 planes in a manner similar to how the use of 100 steps compares with 200.

DOI: 10.1002/nme

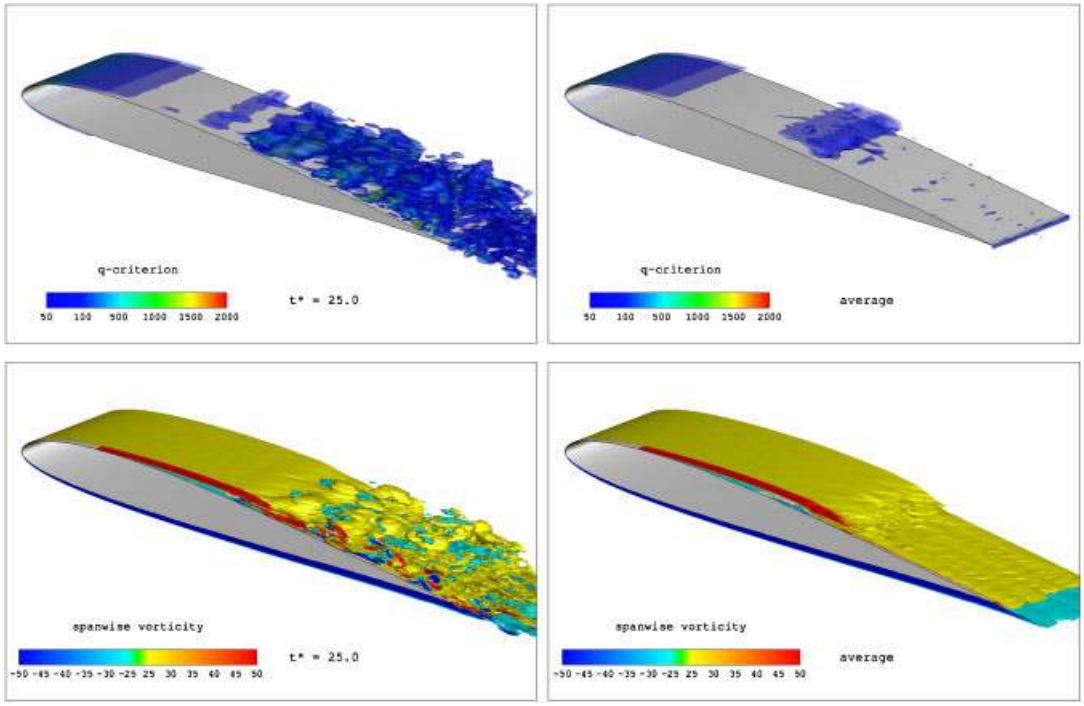

Figure 31. Instantaneous (left) and average (right) iso-surfaces of q-criterion (top) and span-wise vorticity (bottom) at $Re=60\,000$ with grid 2, $p=4$.

Thus, in order to obtain proper averages, the use of 200 solutions and 20 span-wise planes is deemed sufficient, in spite of the small fluctuations observed in the average boundary layer integral lengths after transition. Only for the amplification factor chord-wise evolution these statistics seem inadequate, but still allowed us to observe the TS waves (see Section 6.7).

6.6. Results with grid 2, $p=4$

At $Re=60\,000$, three-dimensional structures are present as made visible by the iso-surfaces of q-criterion and span-wise vorticity of Figure 31. With a fifth-order method, a relatively coarse mesh (grid 2, $p=4$) with 1.8 million high-order nodes is able to accurately capture the average locations of separation, transition, and reattachment, as well as the average pressure and skin friction coefficient profiles along the foil which can be seen in Figure 32—together with comparison curves for the data from XFOIL [36] and by Visbal and coworkers [3, 4] who employ a well-resolved grid with about 4.8 million nodes. The separation bubble is clearly visible in these profiles, with separation occurring on average at 21% of the chord and reattachment at 67% in the present simulations. As expected, the length of the LSB is significantly shorter ($0.46c$ compared to $0.72c$) than at $Re=22\,000$ due to a more rapid transition.

Table VI gives a comparison with previously published results, as well as the transition location and the mean lift and drag coefficients, while Table VII provides the results at the three Reynolds numbers considered. TU-BS corresponds to the PIV experiments at the Technical University of Braunschweig Low-Noise Wind Tunnel [38], whereas HFWT is from the PIV experiments at the Air Force Research Laboratory Horizontal Free-Surface Water Tunnel [15]. The present results are well within variations between previously published works.

Contours of instantaneous and average span-wise vorticity are shown in Figure 33, and reveal a large number of small structures created by turbulent motions past the mid-chord. The laminar separation bubble is clearly visible from the average streamlines in Figure 35. Average non-dimensional velocity correlations can be seen in Figure 34 and illustrate the presence of transition to turbulence. This is verified by looking at the displacement thickness, momentum thickness, and

DOI: 10.1002/nme

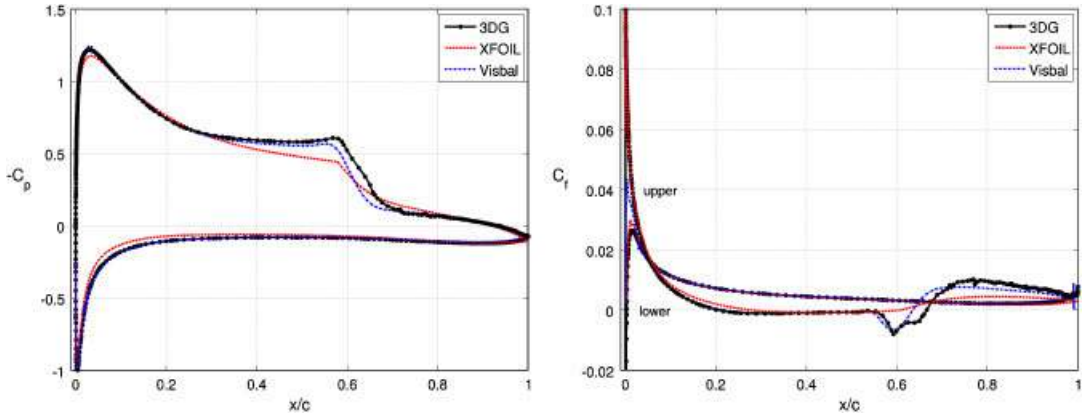

Figure 32. Average pressure coefficient (left) and stream-wise skin friction coefficient (right) at $Re=60\,000$ on grid 2, $p=4$. The dashed lines give XFOIL predictions at 3.37°, $N_{\text{crit}}=7$. The dot-dashed lines show the ILES data of Visbal *et al.* [3, 4].

Table VI. Comparison of results at Reynolds 60 000 with grid 2, $p=4$. The XFOIL data is for 3.37° angle of attack; TU-BS [38] and HFWT [15] correspond to PIV experiments; Visbal *et al.* [3, 4] is an ILES.

Source	Freestream turbulence	Separation x_{sep}/c	Transition x_{tr}/c	Reattachment x_{r}/c	Bubble length	$\overline{C_{\text{L}}}$	$\overline{C_{\text{D}}}$
TU-BS [38]	0.08 %	0.30	0.53	0.62	$0.32c$	—	—
HFWT [15]	$\sim$0.1%	0.18	0.47	0.58	$0.40c$	—	—
Visbal [3, 4]	0	0.23	0.55	0.65	$0.42c$	—	—
XFOIL	($N_{\text{crit}}=7$)	0.28	0.58	0.61	$0.34c$	0.5624	0.0176
present ILES	0	0.21	0.53	0.67	$0.46c$	0.6122	0.0241

Table VII. Summary of results at the three Reynolds numbers considered with: grid 1, $p=3$ for $Re=10\,000$; grid 2, $p=3$ for $Re=22,000$; grid 2, $p=4$ for $Re=60\,000$.

Reynolds number	Separation x_{sep}/c	Transition x_{tr}/c	Reattachment x_{r}/c	Bubble length	$\overline{C_{\text{L}}}$	$\overline{C_{\text{D}}}$
10 000	0.3557	0.9384	—	—	0.3743	0.04967
22 000	0.2386	0.6812	0.9379	$0.6993c$	0.6456	0.04272
60 000	0.2069	0.5335	0.6658	$0.4589c$	0.6122	0.02407

shape factor of the pseudo-velocity profile (Figure 36). A sharp peak in shape factor reveals that transition to turbulence occurs on average at 53% of the chord.

6.7. *Transition mechanism*

The profiles of fluctuating stream-wise pseudo-velocity, $\overline{u_1'^2}/\overline{u_e^2}$, can be seen on Figure 37, for chord-wise stations $x/c\in[0.1, 0.3]$. As for the $Re=22\,000$ flow, each profile is consistent with TS modes, and we observe an increase in perturbation amplitude along the chord-wise direction. The average stream-wise pseudo-velocity profiles look similar to those at $Re=22\,000$ in Figure 21.

The growth of the stream-wise amplification factor along the chord-wise direction can be seen in Figure 38. As mentioned previously, the fluctuations observed from the separation location on ($x/c\geqslant 0.24$) indicate that the temporal averages need to be carried out over a longer period of time. The dotted line shows the amplification factor of the single most energetic wave as predicted by

DOI: 10.1002/nme

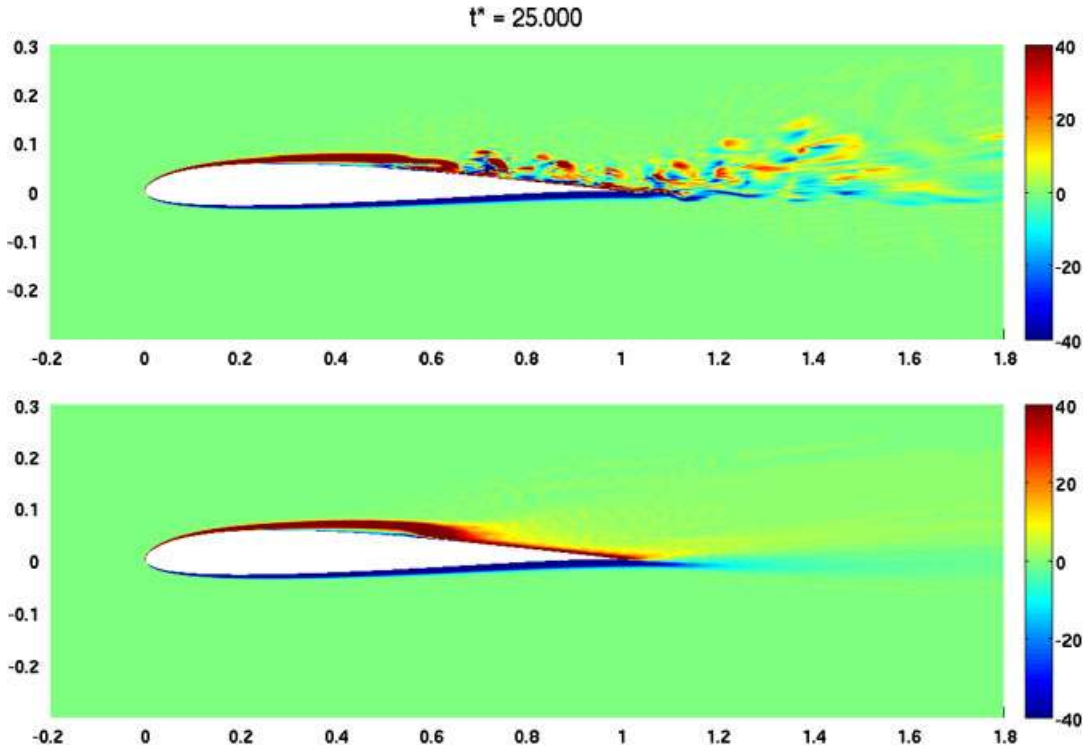

Figure 33. Span-wise vorticity at $Re = 60000$ with grid 2, $p = 4$: instantaneous span-wise average (top) and average (bottom) contours.

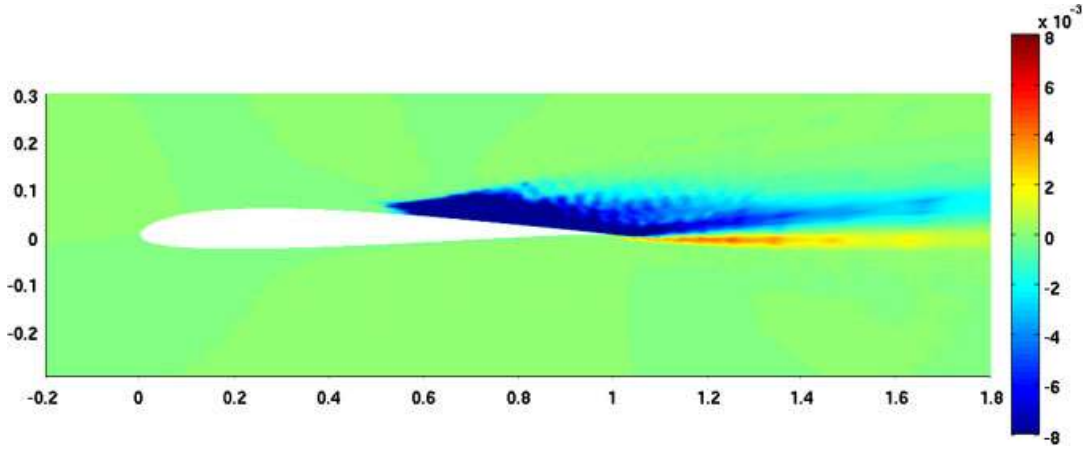

Figure 34. Non-dimensional streamwise-transverse velocity correlations $\overline{u'_s u'_t}/U_\infty^2$ at $Re = 60000$ with grid 2, $p = 4$.

XFOIL, while the solid line for the present simulation is the result of the integration (18) and hence corresponds to the compounded energy of all the waves; this explains why the XFOIL line gives a smaller amplification factor at any given location. However, the slopes of the lines for both cases are very similar, which confirms that the unstable modes are properly captured even with the relatively coarse grid used.

Again, both the shape of the fluctuating stream-wise pseudo-velocity profiles and the spatial growth of the amplification factor indicate that the mechanism of transition along the LSB for these low Reynolds number flows is a TS natural transition.

DOI: 10.1002/nme

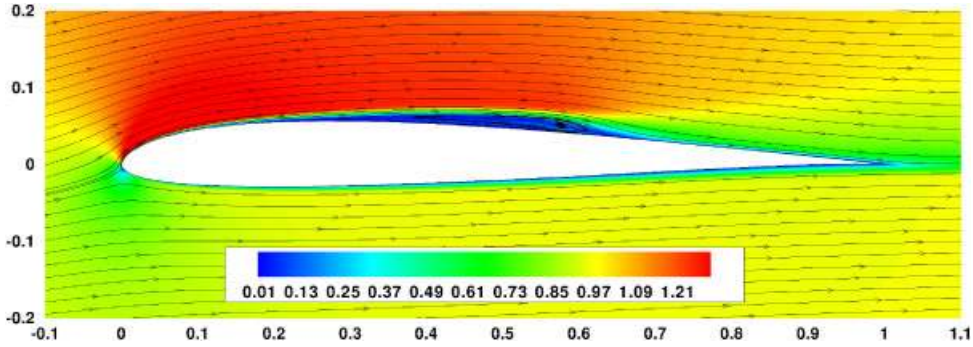

Figure 35. Average streamlines at $Re = 60000$ with grid 2, $p = 4$, and contours of velocity magnitude.

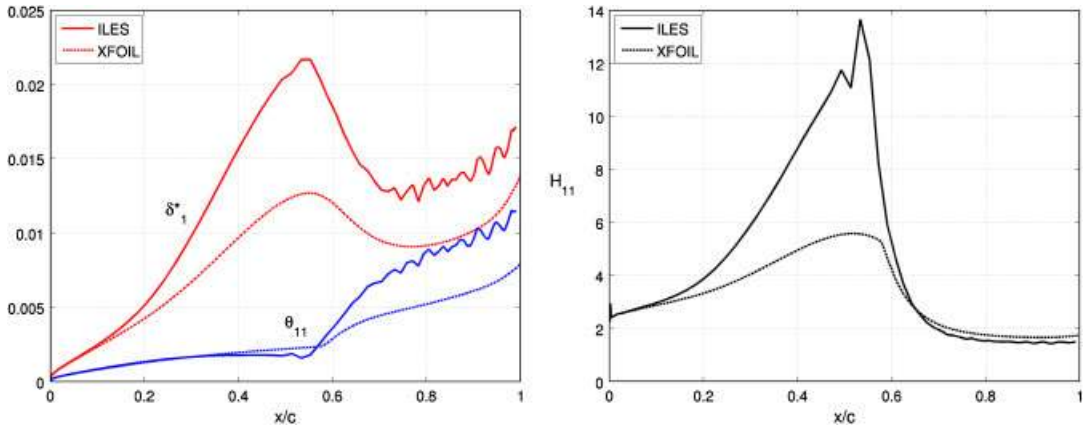

Figure 36. Boundary layer average stream-wise displacement and momentum thicknesses (left), and shape factor (right) evolution along the chord-wise direction at $Re = 60000$ with grid 2, $p = 4$. The dashed lines give XFOIL predictions at 3.37° angle of attack, $N_{\text{crit}} = 7$.

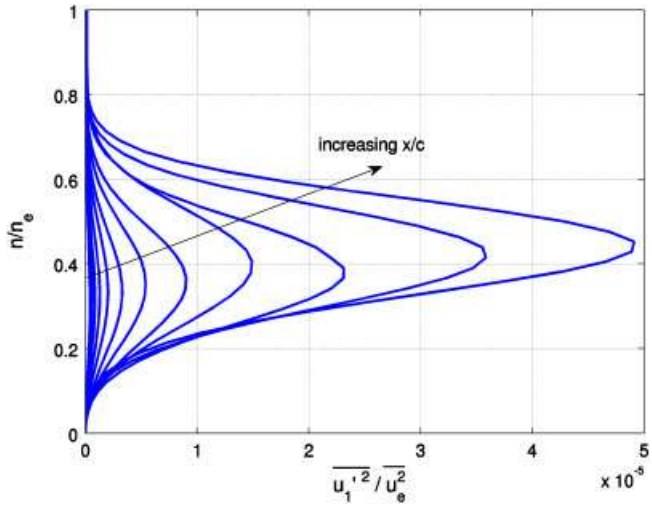

Figure 37. Boundary layer average fluctuating stream-wise pseudo-velocity profiles $\overline{u_1'^2}/\overline{u_e^2}$ at different chord-wise locations $x/c \in [0.1, 0.3]$ at $Re = 60000$ with grid 2, $p = 4$.

DOI: 10.1002/nme

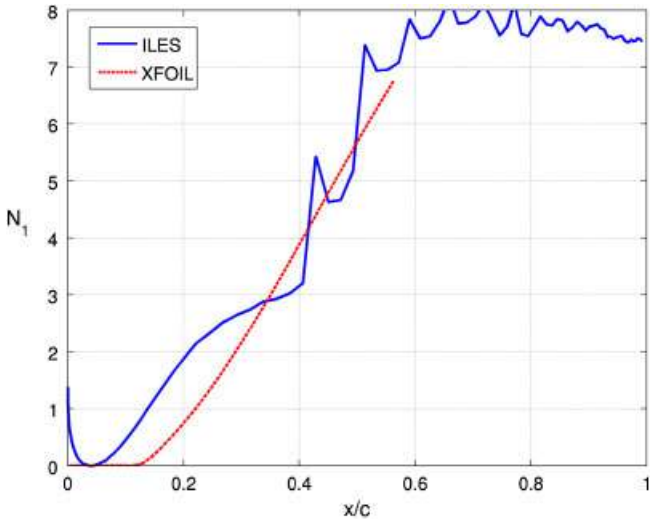

Figure 38. Amplification factor N_1 of stream-wise pseudo-velocity perturbations for the flow at $Re = 60\,000$ with grid 2, $p = 4$.

7. CONCLUSIONS

This paper shows how the formation and related transition to turbulence of an LSB on an SD7003 infinite wing at 4° angle of attack and low Reynolds numbers can be predicted by means of an ILES using a DG method with relatively coarse grids. Attention is given to the boundary layer characteristics that had not yet been previously studied using numerical simulations of this problem.

At $Re = 10\,000$, the flow is found to be two-dimensional with no closed LSB formation (no reattachment) and a periodic shedding of pairs of counter-rotating vortices. For this flow, computations with 430 080 high-order nodes and polynomials of order $p = 3$ are sufficient, and two-dimensional simulations provide a good estimate.

At the higher Reynolds numbers of 22 000 and 60 000, significant three-dimensional effects are present and an LSB is observed on the upper surface. In order to capture the main flow features, close to 1 million high-order nodes are required with $p = 3$ at $Re = 22\,000$, whereas at $Re = 60\,000$ about 1.8 million nodes and $p = 4$ are necessary. The study of transition that takes place along the LSB, through the boundary layer stream-wise fluctuating pseudo-velocity profiles and the spatial growth of the amplification factor, shows that the transition taking place is due to unstable TS waves and hence a natural transition. This observation of TS waves through numerical simulations has not been evidenced in other works.

Further work focuses on swept wings with cross-flow and on a pitching and/or heaving infinite wing at low Reynolds numbers as required for the design of MAVs. The question of how well the numerical dissipation in a DG method functions as an implicit SGS model for ILES is still unclear, and the present work being the first to use DG for ILES provides only a limited insight; contributing to the understanding of this matter will also be the purpose of future investigations.

ACKNOWLEDGEMENTS

The authors acknowledge the support for this work provided by the Air Force Office of Scientific Research under the Multi-University Research Initiative project 'Biologically Inspired Flight' under grant number 001425594000. Furthermore, A. Uranga is thankful for the scholarship provided by Mexico's National Council for Science and Technology (CONACYT). The authors also thank M. Galbraith and M. Visbal for providing their computational data for comparison.

This research was supported in part by the National Science Foundation through TeraGrid resources provided by the Texas Advanced Computing Center, the National Center for Supercomputing Applications,

DOI: 10.1002/nme

and the Louisiana Optical Network Initiative under grant number TG-ASC080034N. It also used the Lawrencium computational cluster resource provided by the IT Division at the Lawrence Berkeley National Laboratory (Supported by the Director, Office of Science, Office of Basic Energy Sciences, of the U.S. Department of Energy under Contract No. DE-AC02-05CH11231).

REFERENCES

1. Uranga A, Persson P-O, Drela M, Peraire J. Implicit Large Eddy Simulation of transitional flows over airfoils and wings. *Nineteenth AIAA Computational Fluid Dynamics Conference*, San Antonio, TX, 22–25 June 2008, AIAA-2009-4131, 2009.
2. Zang Y, Street RL, Koseff JR. A dynamic mixed subgrid-scale model and its application to turbulent recirculating flows. *Physics of Fluids A* 1993; **5**(12):3186–3196.
3. Galbraith MC, Visbal MR. Implicit Large-Eddy Simulation of low Reynolds number flow past the SD7003 airfoil. *Forty-sixth AIAA Aerospace Sciences Meeting and Exhibit*, Reno, NV, 7–10 January 2008, AIAA-2008-225, 2008.
4. Visbal MR, Gordnier RE, Galbraith MC. High-fidelity simulations of moving and flexible airfoils at low Reynolds numbers. *Experiments in Fluids* 2009; **46**:903–922.
5. Scott Collis S. The DG/VMS method for unified turbulence simulation. *Thirty-second AIAA Fluid Dynamics Conference and Exhibit*, St. Louis, MO, 24–26 June 2002, AIAA-2002-3124, 2002.
6. Ramakrishnan S, Scott Collis S. Multiscale modeling for turbulence simulation in complex geometries. *Forty-second AIAA Aerospace Sciences Meeting and Exhibit*, Reno, NV, 5–8 January 2004, AIAA-2004-241, 2004,
7. Sengupta K, Mashayek F. Large-eddy simulation using a discontinuous Galerkin spectral element method. *Forty-fifth AIAA Aerospace Sciences Meeting and Exhibit*, Reno, NV, 8–11 January 2004, AIAA-2007-402, 2007.
8. Xu Z, Stanescu D, Naughton JW. Development of a spectral element DNS/LES method for turbulent flow simulations. *Fifth Joint ASME/JSME Fluids Engineering Conference*, *FEDSM 2007*, San Diego, CA, 30 July–2 August 2007.
9. Alam M, Sandham ND. Direct Numerical Simulation of 'short' laminar separation bubbles with turbulent reattachment. *Journal of Fluid Mechanics* 2000; **41**:1–28.
10. Lang M, Rist U, Wagner S. Investigations on controlled transition development in a laminar separation bubble by means of LDA and PVI. *Experiments in Fluids* 2004; **36**(1):43–52.
11. Hain R, Kähler CJ, Radespiel R. Dynamics of laminar separation bubbles at low-Reynolds-number aerofoils. *Journal of Fluid Mechanics* 2009; **630**:129–153.
12. Drela M, Giles MB. Viscous-inviscid analysis of transonic and low Reynolds number airfoils. *AIAA Journal* 1987; **25**(10):1347–1355.
13. Selig MS, Donovan JF, Fraser DB. *Airfoils at Low Speeds*. Soartech 8, H.A. Stokely Publisher: Virginia Beach, VA, U.S.A., 1989.
14. Selig MS, Guglielmo JJ, Broeren AP, Giguere P. *Summary of Low-speed Airfoil Data*. Soartech Aero Publications, H.A. Stokely: Virginia Beach, VA, U.S.A., 1995.
15. Ol M, McAuliffe BR, Hanff ES, Scholz U, Kahler C. Comparison of laminar separation bubbles measurements on a low Reynolds number airfoil in three facilities. *Proceedings of the 35th Fluid Dynamics Conference and Exhibit*, Toronto, Ont., Canada, AIAA-2005-5149, 2005.
16. Tang L. RANS simulation of a low-Reynolds-number airfoil aerodynamics. *Forty-fourth AIAA Aerospace Sciences Meeting and Exhibit*, Reno, NV, 9–12 January 2006, AIAA-2006-249, 2006.
17. Lian Y, Shyy W. Laminar-turbulent transition of a low Reynolds number rigid or flexible airfoil. *AIAA Journal* 2007; **45**(7):1501–1513.
18. Qin S, Zhuang M, Visbal MR, Galbraith MC, Lian Y, Shyy W. Local and global stability analysis on flows around a SD7003 airfoil. *Forty-seventh AIAA Aerospace Sciences Meeting*, Orlando, FL, 5–8 January 2009, AIAA-2009-1470, 2009.
19. Lesieur M, Métais O. New trends in Large-Eddy Simulations of turbulence. *Annual Review of Fluid Mechanics* 1996; **28**:45–82.
20. Meneveau C, Katz J. Scale-invariance and turbulence models for Large-Eddy Simulation. *Annual Review of Fluid Mechanics* 2000; **32**:1–32.
21. Spalart PR. Strategies for turbulence modelling and simulations. *International Journal of Heat and Fluid Flow* 2000; **21**:252–263.
22. Fureby C, Taylor G, Weller HG, Gosman AD. A comparative study of subgrid scale models in homogeneous isotropic turbulence. *Physics of Fluids* 1997; **9**(5):1416–1429.
23. Boris JP. On Large Eddy Simulation using subgrid turbulence models. In *Whither Turbulence*? *Turbulence at the Crossroads*, Lumley JL (ed.). Springer: New York, 1990; 344–353.
24. Drikakis D, Marco H, Grinstein FF, DeVore CR, Fureby C, Liefvendahl M, Youngs DL. Numerics for ILES: limiting algorithms. In *Implicit Large-Eddy Simulation*: *Computing Turbulent Flow Dynamics*, Grinstein FF, Margolin LG, Rider WJ (eds). Cambridge University Press: New York, NY, U.S.A., 2007; 94–129.
25. Grinstein FF, Margolin LG, Rider WJ. A rationale for implicit LES. In *Implicit Large-Eddy Simulation*: *Computing Turbulent Flow Dynamics*, Grinstein FF, Margolin LG, Rider WJ (eds). Cambridge University Press: New York, NY, U.S.A., 2007.

DOI: 10.1002/nme

26. Margolin LG, Rider WJ. Numerical regularization: the numerical analysis of implicit subgrid models. In *Implicit Large-Eddy Simulation*: *Computing Turbulent Flow Dynamics*, Grinstein FF, Margolin LG, Rider WJ (eds). Cambridge University Press: New York, NY, U.S.A., 2007; 195–221.
27. Fureby U, Grinstein FF. Monotonically integrated Large Eddy Simulation of free shear flows. *AIAA Journal* 1999; **37**:544–556.
28. Fureby C, Grinstein FF. Large-Eddy Simulation of high Reynolds-number free and wall bounded flows. *Journal of Computational Physics* 2002; **181**:68.
29. Rider WJ, Margolin LG. From numerical analysis to implicit subgrid turbulence modeling. *Sixteenth AIAA Computational Fluid Dynamics Conference*, Orlando, FL, 23–26 June 2003, AIAA-2003-4101, 2003.
30. Grinstein FF, Margolin LG, Rider WJ. Introduction. In *Implicit Large-Eddy Simulation*: *Computing Turbulent Flow Dynamics*, Grinstein FF, Margolin LG, Rider WJ (eds). Cambridge University Press: New York, NY, U.S.A., 2007; 1–6.
31. Roe PL. Approximate Riemann solvers, parameter vectors, and difference schemes. *Journal of Computational Physics* 1981; **43**(2):357–372.
32. Peraire J, Persson P-O. The Compact Discontinuous Galerkin (CDG) method for elliptic problems. *SIAM Journal of Scientific Computing* 2008; **30**(4):1806–1824.
33. Persson P-O, Peraire J. Newton-GMRES preconditioning for Discontinuous Galerkin discretizations of the Navier-Sstokes equations. *SIAM Journal on Scientific Computing* 2008; **30**(6):2709–2733.
34. Persson P-O. Scalable parallel Newton–Krylov solvers for Discontinuous Galerkin discretizations. *Proceedings of the 47th AIAA Aerospace Sciences Meeting and Exhibit*, Reno, Nevada, AIAA-2009-606, 2009.
35. Alexander R. Diagonally implicit Runge–Kutta methods for stiff O.D.E.'s. *SIAM Journal on Numerical Analysis* 1977; **14**(6):1006–1021.
36. Drela M. *XFOIL Users Guide*, *Version 6.94*. MIT Aeronautics and Astronautics Department, 2002.
37. Dubeif Y, Delcayre F. On coherent-vortex identification in turbulence. *Journal of Turbulence* 2000; **1**(11):1–22.
38. Radespiel R, Windte J, Scholz U. Numerical and experimental flow analysis of moving airfoils with laminar separation bubbles. *AIAA Paper 2006-501*, January 2006.

DOI: 10.1002/nme